




Article

Coupled Stratospheric Chemistry-Meteorology Data Assimilation. Part I: Modeling chemistry-dynamics interactions

Richard Ménard ^{1,†,*} , Simon Chabrilat ^{2,†} , Alain Robichaud ¹, Jean de Grandpré ¹, Martin Charron ³, Yves Rochon ¹, Rebecca Batchelor ⁴ , Alexander Kallaur ¹, Mateusz Reszka ⁵, and Jacek W. Kaminski ⁶

¹ Air Quality Research Division, Environment and Climate Change Canada, Montréal, Canada

² Belgium Institute for Space Aeronomy, Brussels, Belgium

³ Meteorological Research Division, Environment and Climate Change Canada, Montréal, Canada

⁴ Department of Physics, University of Toronto, Canada, now at University of Puerto Rico Humacao, Puerto Rico, USA

⁵ Data Assimilation and Quality control Section, Canadian Center for Meteorological and Environmental Prediction

⁶ Institute of Geophysics, Polish Academy of Sciences, Warsaw, Poland

* Correspondence: 2121 Transcanada Highway, Dorval (QC), H9P 1J3, CANADA, richard.menard@canada.ca; Tel.: +1-514-421-4613

† These authors contributed equally to this work.

Abstract: A coupled stratospheric chemistry-meteorology model was developed by combining the Canadian operational weather prediction model Global Environmental Multiscale (GEM) with a comprehensive stratospheric photochemistry model from the Belgian Assimilation System for Chemical Observations (BASCOE). The coupled model was called GEM-BACH for GEM-Belgian Atmospheric Chemistry. The coupling was made across a chemical interface that preserves time splitting while being modular, allowing GEM to run with or without chemistry. An evaluation of the coupling was performed by comparing the coupled model, refreshed by meteorological analyses every 6 hours, against the standard offline chemical transport model (CTM) approach. Results show that the dynamical meteorological consistency between meteorological analysis times far outweighs the error created by the jump resulting from the meteorological analysis increments at regular time intervals, irrespective whether a 3D-Var or 4D-Var meteorological analysis is used. GEM-BACH forecast refreshed by meteorological analyses every 6 hours were compared against independent measurements of temperature, long-lived species, ozone and water vapor. The comparison showed a relatively good agreement throughout

the stratosphere except for an upper-level warm temperature bias and an ozone deficit of nearly 15%. Arguments in favor of using the same horizontal resolution for chemistry, meteorology, and meteorological analysis increments are also presented. In particular, the coupled model simulation during an ozone hole event gives better ozone concentrations than a 4D-Var chemical assimilation at a lower resolution.

Keywords: Coupled chemistry-meteorology model; dynamical-photochemical-radiation interactions in the stratosphere; comparison between online model and off-line CTM approach

1. Introduction

The stratosphere is rich in dynamical-photochemical-radiation interactions [1]. It has been monitored over several decades by a number of research satellite missions that provided, for the most part, height-resolved measurements of chemical composition and temperature in the form of limb soundings (a technique in which the satellite view is tangent to the atmosphere). Important missions began in the early 1990's with the Upper Atmosphere Research Satellite (UARS) [2–4] followed by the Environmental Satellite Envisat [5–7] and NASA's Earth Observing System (EOS) Aura [8–10]. Considering these interactions and the quality of stratospheric observations available, we have conducted a study, the ultimate goal of which is to address the question "*To what extent does the assimilation of chemical observations, and in particular those provided by limb measurements, impact the meteorology, in particular on time-scales relevant to numerical weather prediction?*". In this part of the study, referred as Part I, we focus on the development and validation of a coupled meteorology-chemistry model by extending the Canadian Meteorological Centre's (CMC) operational numerical weather prediction (NWP) model.

Atmospheric dynamics is chaotic and their model representation is very sensitive to initial conditions. Atmospheric chemistry models are quite different in that aspect; the chemistry is strongly dependent on the meteorology as well as chemical sources and sinks. A free chemistry simulation, without chemical data assimilation but driven by meteorological analyses, can be compared to a reasonable degree of accuracy, to chemical observations at their proper time and location [11].

Traditionally, Chemical Transport Models (CTM's) [12,13] have offered the most complete chemical representation and are often used as benchmarks for chemistry. CTM's are usually driven offline by meteorological analyses. While the meteorological analyses are usually (and practically) only available at 6 or 12 hour time intervals, the meteorology has to be interpolated in time in order to give a dynamical

field to drive the chemistry at each model time step. Clearly a CTM cannot be used to study the impact of the chemistry on the meteorology.

It is interesting to note the complementary nature of Numerical Weather Prediction (NWP) models with CTM's. Indeed, NWP models solve for; a) momentum, b) thermodynamics, c) conservation of mass and aside from water vapor, d) use climatological fields as input for chemical composition (in particular ozone and greenhouse gases). In contrast, CTMs; a) provide a comprehensive representation of chemical composition, b) solve for the conservation of mass of individual species using chemical reactions and photochemistry, c) but require as input the momentum (winds), thermodynamics (temperature) and total mass (surface pressure). NWP models routinely use data assimilation, and a number of CTM's also have (chemical) data assimilation capabilities. By bringing together these two approaches we can develop a fully coupled chemistry-meteorology model with data assimilation capabilities.

Coupled meteorology-chemistry models provide not only a consistent treatment of the processes shared by meteorology and chemistry but also allow for three-way interactions between physical, chemical and radiation processes [14]. Coupled meteorology-chemistry models are used in several areas such as; 1) in climate simulations with Global Chemistry Circulation Models (GCCM's) [15–17] and in climate-chemistry process validation [18,19], 2) for air quality modeling and prediction [20,21], and 3) to examine the impact of chemical composition on weather prediction [14,22]. This wide range of modeling activity is also nicely summarized in a WMO GAW report [23].

The above three classes of coupled models differ somewhat from each other. While GCCM's consider simulations on multi-decadal to century time-scales, air quality models and numerical weather prediction models coupled with air quality focus on time scales of hours to a year. Chemistry-climate models and GCCM's typically have a lower horizontal and vertical resolution than NWP models and generally have limited chemistry composition modeling aimed primarily at simulating GHG (greenhouse gases), aerosols, and aerosol precursors such as those involved in the sulfate cycle (e.g.[24]). When used in process studies (e.g. [19]) or in comparison with observations, these models are usually forced towards meteorological analyses: 1-either by replacing the model dynamical fields by meteorological analyses (which we call *meteorological refresh*) or by *specified dynamics* [16] that consist of a linear relaxation technique to force incrementally the dynamical fields towards linearly interpolated (in time) meteorological analyses (usually called *analysis nudging*) [25]. In both of these cases, the radiation feedback on meteorology cannot be examined.

In contrast, air quality models and NWP models coupled with air quality models (classes 2 and 3 above) focus on shorter time-scales, have higher resolution both horizontally and vertically and have

comprehensive chemistry and aerosol physics and dynamics. Such coupled models allow for the direct assimilation of meteorological observations but are generally used for tropospheric applications [14]. Only a few models were ever used to investigate the meteorology-chemistry-radiation coupling in the stratosphere (e.g. [26] and the model used here). Despite the fact that temperature and winds have an important effect on the chemical transport and composition in the stratosphere, little is known about how chemical composition impacts the meteorology on synoptic time scales (i.e. hours to weeks), with the exception that ozone has an impact on lower stratosphere temperature predictability [27].

In this study we have constructed such a coupled model starting from the Canadian operational meteorological model [28] GEM (Global Environmental Multiscale model), extended it with relevant physical processes in the stratosphere, and combined it with a comprehensive stratospheric chemical transport model, BASCOE (Belgian Assimilation System for Chemical Observations), where advanced variational assimilation and ensemble Kalman filtering methods has been used for chemical data assimilation [29–32]. This coupled model is called GEM-BACH for GEM Belgium Atmospheric CHemistry model.

The organization of Part I can be summarized as follows. First we present the stratospheric coupling between dynamics, radiation and chemical composition (section 2). Then, in section 3, we describe the formulation of the coupled model, what changes were needed, and discuss the modular design of the chemical interface that allows the meteorological model to run with or without chemistry. We then discuss how coupled models and CTM models can be driven by meteorological analyses, discuss their properties and errors, and through a series of experiments we quantify the errors in each formulation. Finally, since chemistry is largely driven by meteorology, we discuss the importance of analysis and model resolution on the accuracy of a simulation and contrast it with lower resolution chemical data assimilation. This leads to important considerations for the assimilation component addressed in the second part of this study.

2. Background on dynamical-photochemical-radiation interactions in the stratosphere

There are two sources of energy which have a profound impact on the temperature and circulation that characterizes the stratosphere; one is of chemical origin and the other of wave/mechanical origin.

A number of tropospheric chemical source species which enter the stratosphere (e.g. O_2 , H_2O , N_2O , CFC's) are photo-dissociated by solar ultraviolet light, producing chemically-active (fast reacting) species (e.g. O , OH , NO , ClO ; see Table 1 for a more complete list). That is the case for molecular oxygen, which is the second most abundant atmospheric gas. O_2 is photo-dissociated at an altitude of about 50 km, resulting in atomic oxygen and very rapidly recombines with molecular oxygen giving rise to

ozone O_3 , and O_3 also recombine with atomic oxygen. These "recombination-type" chemical reactions are exothermic and release so much heat that they transform the vertical stratification of the atmosphere into a deep stable layer from the tropopause up to 50 km, which characterizes the stratosphere. These chemical reactions are known collectively as the Chapman mechanism and are identified with (*) in Table A1 and A3 of Appendix A. The ozone chemistry also involves catalytic loss cycles with the hydrogen (HO_x), nitrogen (NO_x), and halogen (ClO_x , BrO_x) families, which generate other constituents and in particular stable (long-lived) molecules called *reservoir species* (e.g. [33]).

Figure 1 is a diagram of the dynamical-photochemical-radiative interactions in the stratosphere. This major source of heating which is associated with the production of ozone is depicted as a pink arrow in the figure (lower left side). On a global, yearly averaged scale, the heating is nearly counterbalanced by infrared cooling by CO_2 , and by O_3 (about half of the effect of CO_2), with a small contribution due to H_2O [34](see Figure S1 in Supplementary Material).

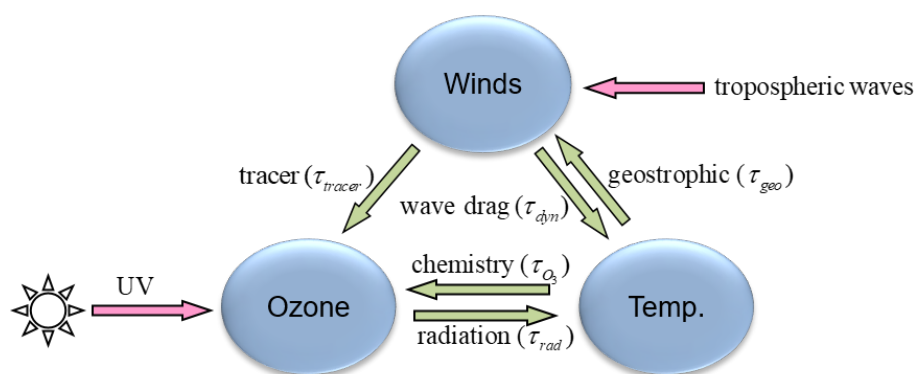


Figure 1. Dynamical-photochemical-radiation interactions in the stratosphere.

The other important source of energy in the stratosphere is mechanically driven by the drag force due to breaking waves of tropospheric origin. In contrast to the troposphere, where diabatic heating creates vertical motion, it is the mechanically driven circulation in the stratosphere which induces vertical motion of which diabatic heating (in isentropic coordinates) is an outcome and not a cause [35,36]. This source of energy is depicted as the second pink arrow in Figure 1 (upper right side).

The wave drag is explained by the breaking of vertically propagating Rossby and gravity waves in the stratosphere [35]. Planetary-scale Rossby waves, which are forced by orography and land-sea contrasts, can propagate upward only in westerly flow and can reach the stratosphere. Depending on the background mean zonal wind and the wavelength, Rossby waves can become stationary and have growing amplitudes. If, in addition, there is shear flow, tongues of potential vorticity [37–40] develop, and show up in chemical tracer fields as filamentary structures with cutoff features when the Rossby wave

is breaking (e.g. as shown with chemical data assimilation [41]). When the waves break, which occurs at the limit of the diffusion length-scale, they transfer their westward momentum to the zonal flow, thus decelerating it – the so called wave drag.

Gravity waves have the property that their amplitude increases with height as a result of the decreasing air density. Gravity waves excited by orography reach their critical (breaking) level in the upper troposphere and lower stratosphere [42], whereas those induced by non-stationary waves (such as in frontal systems) break at higher altitudes and play a major role in the middle-atmosphere general circulation [43,44]. The horizontal scale of these gravity waves are much smaller than the typical resolution of global models and thus both their generation and impact must be parameterized.

The wave drag induces a meridional circulation which changes temperatures in isentropic coordinates. Since angular momentum is conserved, the zonal momentum balances the wave drag, and thus implies a negative mechanical forcing that needs to be compensated by a poleward meridional mass flux due to the Coriolis effect. By mass conservation, the meridional mass flux is also linked to the vertical mass flux, creating a meridional circulation with ascent near the tropics and descent near the poles. This is the Brewer-Dobson circulation [35,36,45,46] (see white arrow Figure S2 in Supplementary Material). The vertical motion across isentropes might seem at first perplexing, but a slow persistent vertical motion can move air parcels across isentropes due to the relaxation effect of radiation. Indeed, if an air parcel is displaced downward at a given location, the immediate response is to warm it adiabatically. Then, as the temperature locally rises above the radiative equilibrium temperature, it experiences infrared cooling, which allows the downward displacement to continue. In an isentropic vertical coordinate system (i.e. in a coordinate based on potential temperature) the vertical velocity simply equals the net diabatic heating. The stratospheric meridional circulation that is driven by forces of tropospheric origin pulls the middle atmosphere away from the radiative equilibrium locally, but not globally on long time scales.

2.1. Ozone-temperature interaction

Ozone and temperature are related through radiation and photochemistry, but each process results in different ozone-temperature correlations and has its own time-scales (see right and left horizontal green arrows in Figure 1). We will discuss first the processes and then their time-scales.

The absorption of solar UV radiation in the production of ozone creates a rapid, local increase in temperature, which pulls the temperature away from radiative equilibrium. The perturbed air parcel then undergoes infrared cooling on a slower time scale, τ_{rad} , and an adjustment towards a new but

higher equilibrium temperature value takes place. Thus, there is a positive correlation between O_3 and temperature because of radiative coupling.

The photochemistry gives a different correlation. Since chemical reaction rates depend on temperature, the ozone production rate increases with decreasing temperature. In terms of absolute value, correlations as high as 0.9 have been reported, based on ozone and temperature measurements from MLS [47] and CRISTA [48]. Several authors have pointed out [47,49–51] that the temperature dependence can be represented by a function of the form,

$$O_3 = B \exp\left(\frac{\Theta}{T}\right) \quad (1)$$

where B and Θ are constants whose values depend on the reactants involved in the photochemistry. Taking the derivative of Equation 1 we get the perturbation equation,

$$\frac{\Delta O_3}{O_3} = -\frac{\Theta}{T^2} \Delta T \quad (2)$$

which shows that temperature perturbations give rise to negatively correlated ozone perturbations.

Let us now discuss the time-scales of the different processes. To estimate the radiative time-scale τ_{rad} we can use the Newtonian cooling approximation to compute the time required to cool an air parcel through IR emission out to space. This approximation is generally valid above ~ 25 km (or 25 hPa) where the radiation exchange between layers can be neglected. For small temperature perturbations, this Cool-to-Space process Q^{CtS} can be written as $Q^{CtS} = Q^{Lw}(T_0) - \alpha(T - T_0)$ where T_0 is a reference temperature near radiative equilibrium, Q^{Lw} is the infrared (IR) emission at T_0 and $\tau_{rad} = 1/\alpha$ is the radiative relaxation time scale. This parameter has been estimated with the GEM-BACH model using a centered finite difference expression $\tau_{rad} = 2\delta T / [Q(T + \delta T) - Q(T - \delta T)]$ [52] and is displayed in the panel (a) of Figure 2 as a function of latitude and height for a given summer day. We note that τ_{rad} decreases with altitude so that a rapid adjustment of the temperature perturbations by the Cool-to-Space process occurs. In the lower stratosphere below (below ~ 20 hPa), the radiative timescale is on the order of one month or more, indicating that the temperature perturbations can accumulate over that time period and consequently produce a significant temperature response. The lower stratosphere is thus sensitive to ozone-radiation perturbations.

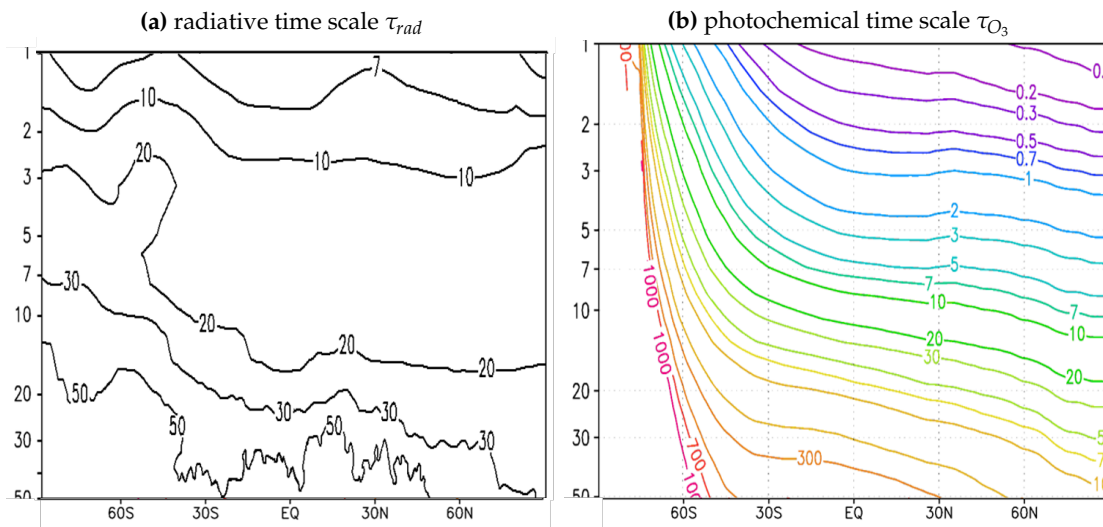


Figure 2. Ozone radiative (left panel) and photochemical time scales (right panel) in days. Latitude vs Pressure (hPa). June first conditions. Note that south of $\sim 70^\circ$ is the polar night.

The ozone photochemical lifetime τ_{O_3} can be defined as the time required for ozone to be reduced by a factor $1/e$ through photochemical reactions. This time scale is readily available from linearized ozone chemistry schemes such as the LINOZ model [53], $dO_3/dt = c_1 + c_2(O_3 - \overline{O_3}) + c_3(T - \overline{T}) + c_4(O_3^\uparrow - \overline{O_3}^\uparrow)$ which represents the tendency of daily mean values. The overbar denotes the climatology, the \uparrow denotes the overhead column of ozone, and the coefficients c_1, c_2, c_3, c_4 are determined using a chemical box model. The photochemical time-scale for ozone is then $\tau_{O_3} = 1/c_2$, which is plotted in panel (b) of Figure 2 for June 1st conditions. Note that the region south of 60° S is in polar night, and the photochemical time-scale is infinite.

Comparing the photochemical time-scale τ_{O_3} with the radiative timescale τ_{rad} in sunlight conditions we note that above ~ 10 hPa, $\tau_{O_3} \ll \tau_{rad}$. The ozone-radiation feedback is small because the lifetime of ozone perturbations is too short to have a significant radiative effect. This is the *photochemistry-dominated region*, in which ozone and temperature perturbations are negatively correlated. In this region the assumptions for chemical transport modeling are valid, as there is no need to change the temperatures. Below ~ 10 hPa, we have $\tau_{O_3} \gg \tau_{rad}$ and the ozone behaves as a passive tracer since the photochemistry can be neglected, but the radiative forcing associated with ozone perturbations persists over several weeks. The ozone radiative impact on temperature can be significant even though the radiative forcing itself is small. Thus, below ~ 10 hPa is the *radiation-dominated region* where ozone and temperature perturbations are positively correlated, benefits from a coupled radiation-chemistry model approach.

194 2.2. Temperature-wind interaction

Horizontally, most of the stratosphere is in geostrophic balance, except between about 20°N and 20°S and the upper-stratosphere and mesosphere due to gravity wave breaking. For example, the geostrophic winds derived from satellite observations provided by the CRISTA instrument showed that on a day-to-day basis these winds are remarkably close to the stratospheric winds in the UKMO meteorological analysis [54]. From a dynamical perspective, local perturbations of the horizontal wind and temperature adjust to a balanced state on short time scales (typically less than six hours) by dispersing away fast-moving inertia-gravity waves – a process known as geostrophic adjustment. A scale analysis using the shallow water model reveals that the Rossby number, defined as $R_o = U/fL$, determines the type of adjustment that will take place: when $R_o < 1$, the temperature tends to adjust to the wind field, and when $R_o > 1$, the wind field tends to adjust to the temperature field (f is the Coriolis parameter and L the length-scale of the disturbance). For planetary scale waves, such as vertically propagating Rossby waves that enter the stratosphere, $R_o < 1$ so that the wind field adjusts to the temperature field. On the other hand, gravity waves of tropospheric origin generally have $R_o > 1$, so that the temperature is adjusted to the wind field. Because this adjustment process is mostly completed after six hours, the short term forecast error used in an intermittent assimilation cycle, are in geostrophic balance. In geostrophic balanced flow the vertical rate of change of the wind is related to the horizontal temperature gradient by the so-called *thermal wind relation*,

$$\frac{\partial u}{\partial p} = \frac{R}{fp} \left(\frac{\partial T}{\partial y} \right)_p ; \quad \frac{\partial v}{\partial p} = -\frac{R}{fp} \left(\frac{\partial T}{\partial x} \right)_p , \quad (3)$$

195 where u and v are the zonal and meridional wind components, p is the pressure, R the gas constant, and T
 196 the temperature. The thermal wind relation introduces a three-dimensional coupling between temperature
 197 and winds, and the time scale associated with this coupling is on the order of the geostrophic adjustment
 198 time scale, τ_{geos} (depicted as the slanted leftward green arrow in Figure 1).

199 On a much longer time-scale and as a result of the Brewer-Dobson circulation, the vertical wind and
 200 temperature are also related, but as explained earlier (beginning of section 2), it is the vertical motion,
 201 induced by wave breaking, that determines the temperature distribution. Since the radiation relaxation
 202 takes place on a time-scale which is faster than the residual circulation, the temperature adapts to a new
 203 radiative equilibrium as the fluid particles rise in the tropics or descend in the polar regions. On this slow
 204 time-scale, we thus observe that the vertical motion drives the temperature change and not the reverse. The
 205 time-scale τ_{dyn} appearing in Figure 1 refers to the slow time scale associated with the residual circulation.

2.3. Wind-tracer interaction

Winds drive the transport of chemical species. From a physical point of view, the chemical tracer mixing ratios have no impact on the winds. For ozone there could be an indirect impact through the radiation followed by geostrophic adjustment, but it is known to be a small, second-order effect, considered to be negligible [55,56].

It has also been observed from aircraft, balloon and satellite platforms that long-lived species display compact relationships in concentrations between species. Also, species with very different sources and sinks exhibit nearly identical meridional-vertical isopleth shapes, indicating that it is the atmospheric transport which maintains these relationships. It was argued [57] that if the sources and sinks are sufficiently slow compared with dynamical timescales, then the meridional slopes of mixing ratio isopleth and the compact correlations between different species are determined by quasi-horizontal mixing. Indeed, the tendency to flatten the isopleths that results from quasi-horizontal mixing is larger than the mean overturning circulation (i.e. the Brewer-Dobson circulation), which tends to steepen the isopleths [57,58]. Depending on the process being considered, the time-scales of the tracer-wind relationship occur on a wide range of values; from $U/\Delta x$ if no mixing is considered, to times-scale longer than a few weeks, but smaller than the Brewer-Dobson circulation time-scale.

3. Description of the coupled meteorology-chemistry model

An online stratospheric chemistry-meteorology model was developed starting from a tropospheric version of the Canadian operational NWP model (with a very preliminary stratospheric extension) and from the Belgium stratospheric offline chemical transport model (CTM). Both models were fully validated in their respective environments [28–30,59,60]. The Canadian NWP model GEM (Global Environmental Multiscale model) with a model top at 10 hPa, had been used operationally with a 3D- and 4D-Var assimilation scheme for nearly a decade in Canada. The Belgian CTM had a comprehensive stratospheric chemistry and had been delivering operational 4D-Var chemical analyses and forecasts for several years prior to the start of this study. The Belgian operational chemical analysis and forecast system is known as the BASCOE.

Several changes were made to construct a coupled model which can produce realistic stratospheric meteorological and chemical simulations. Additional stratospheric physical parameterizations were implemented in GEM (see section 3.1) and were later adapted and implemented for operational Numerical Weather Prediction at higher resolution (33 km) by [61]. The chemistry of BASCOE CTM, which used a flux-form semi-Lagrangian method for transport [62], was extracted and implemented through a chemical

interface in GEM. The resulting chemical transport was then a semi-Lagrangian advection. To reduce the cost of simulating polar stratospheric cloud processes, a temperature-dependent parameterization of aerosol quantities was developed, but otherwise retained the full heterogeneous chemistry. The chemical interface, described in section 4, made the model online both from a dynamical and ozone-radiation perspective, but was also modular (e.g. allowed switching between different chemical packages or running without chemistry). The resulting coupled model was named GEM-BACH.

3.1. Stratospheric extension of the meteorological model

GEM is a two time-level semi-Lagrangian fully-implicit non-hydrostatic grid point model [28] which uses either uniform or variable horizontal-resolution grids [63]. An Arakawa C discretization is used in the horizontal and a hybrid vertical coordinate with non-staggered finite differences is used in the vertical (although this has changed in newer versions of GEM [64]). It can also run in either hydrostatic or non-hydrostatic modes [65]. The model solves for horizontal and vertical momentum, thermodynamics, continuity, an arbitrary number of tracers, and in non-hydrostatic mode it also has a prognostic vertical velocity equation. There is no vertical motion condition across the upper and lower boundaries.

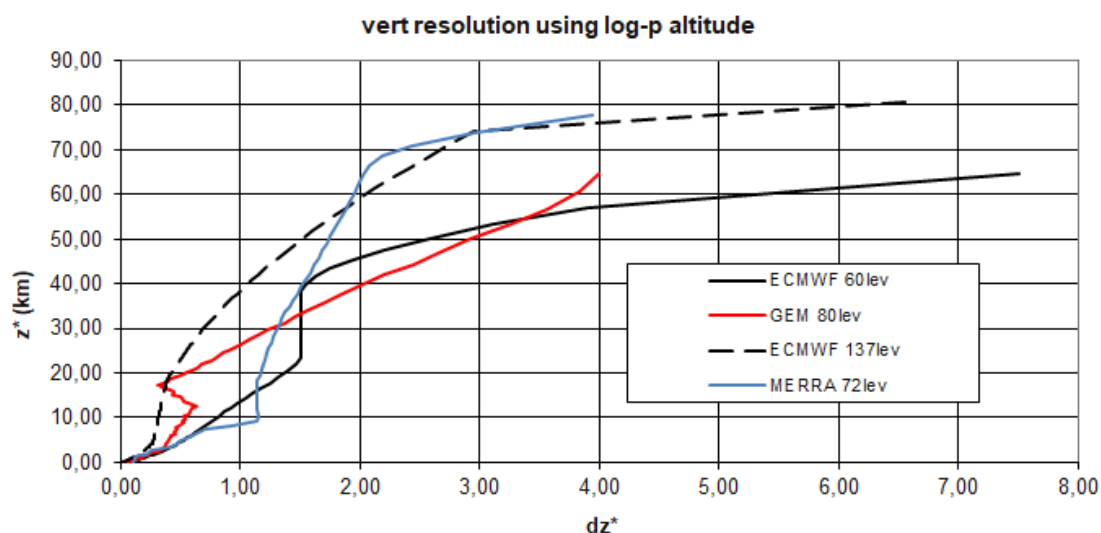


Figure 3. Approximate distributions of the vertical levels of four typical assimilation systems whose domains include the full stratosphere: the ECMWF vertical grid with 60 levels, used for ERA-Interim (black solid line); the ECMWF grid with 137 levels, used operationally and for ERA-5 (black dashed line); the GMAO grid with 72 levels, used for MERRA (blue line) and the GEM or GEM-BACH grid extended to 80 levels which is used here (red line).

The physics used in the tropospheric version of the model includes the following parameterizations [66]; Prediction of surface temperature over land using a force-restore approach; Turbulence in the planetary

boundary layer through vertical diffusion, diffusions based on stability and kinetic energy; Surface layer scheme based on Monin-Obukhov similarity theory; Shallow convection scheme (non-precipitating); Orographic gravity wave drag according to McFarlane [67] and McLandress and McFarlane [42]; Kuo-type deep convection scheme, and the Sundqvist condensation scheme for stratiform precipitation.

For the stratosphere, additional physical parameterizations were added:

- A non-orographic gravity wave drag (GWD) [43,44] scheme. Gravity wave drag induced by the breaking of non-stationary waves generally occurs at higher altitudes and plays a major role in the middle atmosphere general circulation. A Doppler-spread parameterization scheme is used for representing the effects on the middle and upper atmosphere of a spectrum of unresolved gravity waves emerging from a variety of sources.
- A radiation scheme using the correlated-k distribution method [68]. This method is an efficient way to compute the radiation with only a few absorption coefficients and yet it is equivalent to the computation of tens of thousands coefficients in a rigorous line-by-line calculation. The radiation scheme computes the heating and cooling rates due to emission in the IR and absorption in the IR, visible and UV parts of the spectrum. The model can deal with sulfate aerosols, sea salt and dust aerosols, based on published parameterizations for aerosol optical properties [68–72]. This scheme can deal with the following gases interactively with 3-dimensional inputs, H₂O, CO₂, O₃, N₂O, CH₄, CFC-11, CFC-12, CFC-113, and CFC-114.

In addition, and only if GEM runs as a stand-alone meteorological model, i.e. without the BASCOE stratospheric chemistry, we have added

- A new climatology for O₃ following Paul et al. [73] below 0.5 hPa and using HALOE observations above 0.5 hPa. This climatology is one of the key inputs for the radiation scheme. Alternatively, the prognostic ozone modeled with the BASCOE chemistry package can also be used as input to the radiation scheme.
- Water vapor related to meteorological and to chemical processes is treated as two different variables in the coupled model. For the meteorological variable, chemical production and loss of water vapor in the stratosphere is obtained from a parameterization of methane oxidation and water vapor photolysis, which was developed at ECMWF [74] and is based on the observation that total hydrogen is nearly uniform throughout the middle atmosphere [75]. As for the chemical variable, in the stratosphere water vapor is treated as all other chemical species present in the BASCOE

scheme, and in the troposphere it is copied from the meteorological variable. Note that the radiative heating/cooling rate due to water vapor is computed from the meteorological variable.

For this study, both GEM and GEM-BACH are configured to run in hydrostatic mode with a global uniform resolution of $1.5^\circ \times 1.5^\circ$, i.e. 240×120 grid points. The vertical domain extends to 0.1 hPa and uses 80 vertical levels, 27 of which are in the stratosphere. Such high vertical resolution is uncommon to most Global Chemistry Climate Models (GCCM's) which is a distinctive feature of the coupled model GEM-BACH. Figure 3 compares the vertical grid used in this study with the ECMWF vertical grid used back in 2005 (at the beginning of this study). Altitude and vertical grid spacing are estimated using log-pressure altitudes ($z^* = H \ln(p_0/p)$), where the surface pressure p_0 is set to 1000 hPa and the scale height H is set to 7 km.

A series of climate simulations with all four additional physical parameterizations (outlined above) was performed and the results were compared against either ERA 40 climatology or observations (see Figures S3-S5 in the Supplementary Material). We observed that the native run, which is a version of the model with a top at 0.1 hPa but with no additional physical parameterizations, exhibit a tropical tropopause and polar winter stratosphere which were too cold while the summer pole stratosphere was too close to radiative equilibrium. But with these additional parameterizations these issues were significantly corrected compared with the ERA 40 reanalysis. Corrections to the zonal winds were also observed with these additional parameterizations (Figure S4 Supplementary Material), where the Hines GWD scheme reduced the mesospheric jets and the new radiation scheme intensified the zonal wind in the stratosphere. The representation of interannual variability in the zonal winds, obtained from a zonal wind time series in the tropics, was also reasonably well captured with these additional parameterizations (Figure S5 in Supplementary Material).

3.2. Stratospheric chemistry model

The photochemical module that has been implemented in GEM-BACH is the one used by the Belgian Institute for Space Aeronomy (BIRA) which includes 57 species, interacting through 143 gas-phase reactions, 48 photolysis reactions and 9 heterogeneous reactions. Table 1 gives the list of species and Appendix A details the list of photochemical reactions. Appendix B explains the physics of the photochemical reaction rates, the so-called J values. Appendix C gives the lower chemical boundary condition at 400 hPa, the level below which the chemistry solver is not active. The chemical reaction rates and photodissociation rates follow the Jet Propulsion Laboratory compilation [76]. A complete description

of the stratospheric chemistry is not intended to be covered here, and we refer the interested reader to appropriate review papers (e.g. [33]).

Table 1. List of chemical species in BASCOE

Source species	
Natural	H ₂ O, N ₂ O, CH ₄ , CH ₃ Cl, CH ₃ Br
Anthropogenic	CFC-11 (CFCl ₃), CFC-12 (CF ₂ Cl ₂), CFC-113, CFC-114, CFC-115, HA-1301 (CBrF ₃), H-1211 (CBrClF ₂), HCFC-22 (CHClF ₂), CCl ₄ , CH ₃ CCl ₃ , CHClF ₂ , CHBr ₃
Short-lived species	
Oxygen (O _x)	O ₃ , O(¹ D), O(³ P)
Hydrogen (HO _x)	H, OH, HO ₂ , H ₂ O ₂
Nitrogen (NO _x)	N, NO, NO ₂ , NO ₃
Chlorine (ClO _x)	ClOO, OCIO, Cl, ClO, ClONO ₂ , HOCl, Cl ₂ O ₂ , Cl ₂
Bromine (BrO _x)	Br, Br ₂ , BrO, BrCl, HOBr
Hydrocarbons (HC)	CH ₃ , CH ₃ O, CH ₃ O ₂ , CH ₂ O, CH ₃ OOH
Long-lived species	
	HNO ₃ , HNO ₄ , N ₂ O ₅ , ClONO ₂ , BrONO ₂
	HBr, HCl, CO, HF, HCO, H ₂

The rates for gas phase and heterogeneous chemistry depend on temperature. A reaction between two molecules has a reaction rate k_g of the form

$$k_g = Ae^{E/RT}, \tag{4}$$

where E represents the energy of activation, R is the gas constant and A the Arrhenius factor. Reactions involving three molecules can also be pressure-dependent and require more complex formulations. Reaction rates involving aerosols are generally expressed as

$$k_{ae} = \frac{\gamma}{4} \left(\frac{8kT}{\pi M} \right)^{1/2} A_{ae} \tag{5}$$

where the term in parentheses represents the molecular mean speed of the gas-phase molecules, which depends on temperature T , the molecular mass M , and the Boltzman constant k . A_{ae} is the aerosol surface area per unit volume and γ is the reaction efficiency representing the probability that a reaction takes place following the collision of the molecule with the particle. Chemical rate coefficients are determined experimentally and tabulated for different conditions [76].

Heterogeneous chemistry plays an important role, especially in polar regions, and has been explicitly taken into account in GEM-BACH (see table A2). Hydrolysis reactions on the surface of Stratospheric Sulfate Aerosols (SSA) contribute mainly to the removal of active nitrogen in the lower stratosphere. In

polar regions, another important class of aerosols is Polar Stratospheric Clouds (PSC). Such clouds usually form from SSA particles and grow at cold temperatures from the uptake of water vapor and nitric acid (see [77] for a review). In GEM-BACH, the surface area available for heterogeneous reactions is parameterized in a crude manner. Instead of using a costly detailed microphysical calculation, we used a climatology of SSA surface area densities (see Figure S6 in Supplementary Material). Type II PSC particles (primarily composed of water ice) are set to appear at temperatures below 186°K with a surface area density equal to $5 \times 10^{-9} \text{ cm}^2/\text{cm}^3$. Between 186°K and 194°K, they are replaced by Type Ia PSC particles (primarily composed of Nitric Acid Trihydrate, NAT) with the same surface area density. The parameterization of PSCs also incorporates the impact of PSC sedimentation on water vapor (dehydration) and gaseous HNO_3 (denitrification). Exponential losses is prescribed for these two species, with characteristic times of 9 days for water vapor (at the gridpoints where type II PSCs are present) and 100 days for nitric acid (at gridpoints where type Ia PSCs are present).

Since the onset of heterogeneous chemistry on PSC depends on temperature, it is important that the meteorological model is capable of reaching the threshold temperature required. Figure 4 shows the 15-year average temperature over the South Pole region (defined as the area south of 60°S) as function of height and the day of the year. Of course some years are different from others, and the temperature is not completely uniform in the polar vortex, but Figure 4 does indicate that the GEM model reaches temperatures below 190°C.

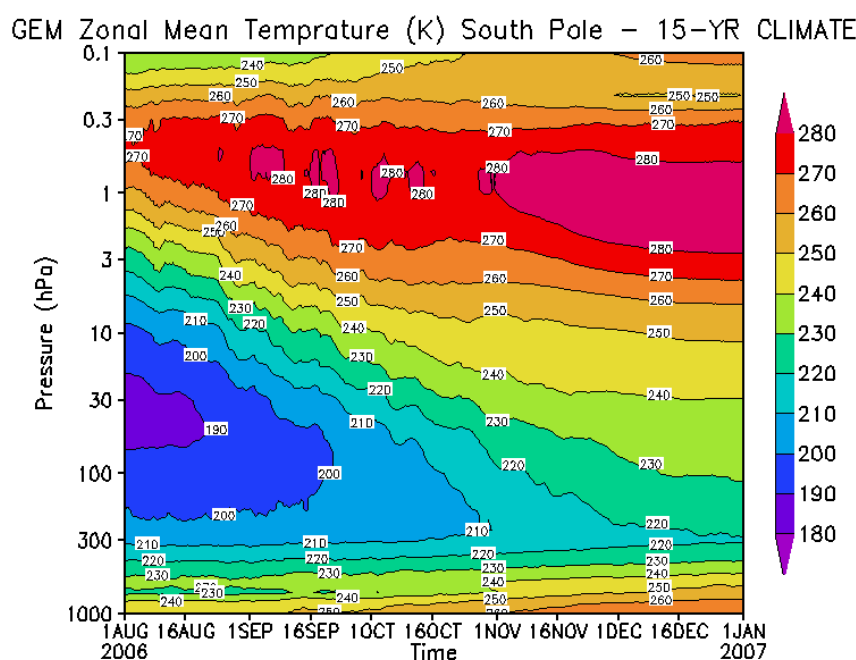


Figure 4. Time series of daily average temperature (over 15 years) over the polar vortex

3.3. Chemical solver

The photochemical module and solver used here follow closely those of [78] used at the Belgian Institute for Space Aeronomy (BIRA). The chemical solver acts on number densities (expressed as molecules- m^{-3}), not on mixing ratios as in transport. Ignoring the issue of advection for the moment, the chemical tendency on a model grid is of the form,

$$\frac{\partial c_i}{\partial t} = P_i(\mathbf{c}) - L_i(\mathbf{c})c_i = \Phi_i(\mathbf{c}), \quad (6)$$

where $\mathbf{c} = (c_1, c_2, \dots, c_J)$ is the vector of number densities for J chemical species, $P(\mathbf{c})$ is the production term and $L(\mathbf{c})$ is the loss term. Together they define, $\Phi_i(\mathbf{c})$, the chemical transformation operator for species i . Equation 6 is obtained by adding all the product and loss processes for each species ($i = 1, \dots, J$) from the list of chemical reactions given in Appendix A. This results in J chemical tendency equations, fewer than the total number of chemical reactions N , ($J < N$). An example of such a procedure is given in Tables 1 and 2 of Yudin and Khattatov (2010) [79]. The photochemical transformation Equation 6 actually forms a set of stiff non-linear equations that span a wide range of chemical time-scales. In principle this is best integrated with an implicit time-discretization scheme (e.g. Backward Euler scheme),

$$\mathbf{c}^{n+1} = \mathbf{c}^n + \Delta t \Phi(\mathbf{c}^{n+1}) \quad (7)$$

which ensures computational stability. However, to deal with the non-linearity of Φ , a linearization around the state at time t_n (up to second order) can be made,

$$\mathbf{c}^{n+1} = \mathbf{c}^n + \Delta t (\Phi(\mathbf{c}^n) + \mathbf{J}(\mathbf{c}^{n+1} - \mathbf{c}^n)), \quad (8)$$

where $\mathbf{J} = \partial \Phi / \partial \mathbf{c}$ is the Jacobian of the chemical production and loss terms, leading to a semi-implicit scheme of the form,

$$\mathbf{c}^{n+1} = \mathbf{c}^n + (\mathbf{I} - \Delta t \mathbf{J})^{-1} \Delta t \Phi(\mathbf{c}^n), \quad (9)$$

which, although it is not guaranteed to be stable, is usually stable in practice. The resulting equation is then linear. The actual numerical scheme that solves the chemistry is a Rosenbrock solver of third-order, that is a variant and generalization of Equation 9, where the time step is subdivided into several internal time steps h (here 3) (see [80], [81] section 16.6, [82]). This solver is made numerically stable through the specification of the coefficient of the Rosenbrock scheme [83]. The Fortran code needed to apply the

Rosenbrock solver for the chemical kinetic equations can be built by the Kinetic PreProcessor (KPP) [84] that also determines the appropriate magnitude of h based on a tolerance factor set as 0.1 in the current version of the model. The chemical solver is applied from the model lid to 400 hPa due to the lack of tropospheric chemistry in the model. In the three bottom layers, species mixing ratios are specified to a set of values taken from the SLIMCAT CTM [13] and are shown in table A.4 in Appendix C. Species vertical fluxes are null at the model lid.

The execution of the chemistry solver with a semi-Lagrangian transport scheme proceeds as follows. First, a semi-Lagrangian advection is performed on all species by interpolating from the upstream (i.e. departure) points to compute the mixing ratio at the arrival point on the model grid. Note that all species have the same upstream point and interpolation weights, which calculated only once. This represents a significant computational savings for the chemical transport. The species mixing ratio is converted into number density and the photochemical tendency for each species is computed on each model grid point. Once the number densities are updated, they are transformed back into mixing ratios for another transport time step or for a call to the physics scheme. The transformation from number density to mixing ratio follows the expression $\chi = (R_* T / N_A p) c$, where T is the temperature, p the pressure, R_* the universal gas constant, and N_A the Avogadro number.

4. Model coupling and interface

Models are composed of several processes which are integrated either sequentially or in parallel (simultaneously). In sequential processing, for a given time step, the model state is updated after each process and provides input to the next process, until all processes are integrated. Sequential processing is also called time splitting. In parallel processing, the tendencies of each process are computed simultaneously using the same initial model state. The updated state is computed from the sum of tendencies. Parallel processing is also called process splitting.

Parallel processing is appealing because of its simplicity and ease of implementation for coupled models. However, it has the disadvantage that the stationary solution of the time-discrete equation does not match the stationary solution of the time-continuous equation [85,86]. Sequential processing doesn't have this problem - it has the same stationary solution as the time-continuous equation. However, the transient solution depends on the order in which the different processes are integrated. The total error is minimized when the processes are ordered from the slowest process to the fastest [87,88].

The meteorological model GEM uses sequential processing and we have followed closely the same approach for the coupled meteorology-chemistry model configuration. In addition, we have adopted a

modular design such that the chemistry component can be present (or not) through a chemical interface. This flexibility allows having a meteorology-only or meteorology-chemistry model configuration. However, this flexibility entails a small additional computational cost and maintenance, since some physics routines need to be duplicated and present in the chemical module. To make this clear let us begin by discussing what sequential processing would look like if chemistry was completely integrated with the physics module.

The processes in the meteorological model GEM are updated in the following sequence: 1 - Radiation, 2 - Advection, 3 - Dynamics terms of meteorological variables using a semi-implicit scheme, 4 - Surface fluxes and gravity wave drag (orographic and non-orographic), 5 - Boundary layer processes and vertical diffusion, 6 - Shallow convection, 7 - Deep convection, and 8 - Microphysics. A coupled meteorology chemistry model has a 9th process - Chemistry, which involves very fast process that in principle should be solved implicitly but in practice we have chosen to use a semi-implicit approach using a Rosenbrock solver (see section 3.3). For the purpose of this discussion let us consider only those processes that involve both meteorological and chemical variables. For stratospheric chemistry those are: 1 - Radiation, 2- Advection, 5 - Vertical diffusion, and 9- Chemistry.

Let \mathbf{X} represent the coupled (augmented) state vector, i.e.

$$\mathbf{X} = \begin{pmatrix} \boldsymbol{\mu} \\ \boldsymbol{\chi} \end{pmatrix} \quad (10)$$

where $\boldsymbol{\mu}$ is the meteorological state vector and $\boldsymbol{\chi}$ the chemical state vector. Then the evolution that matters for the coupled state vector takes the form

$$\frac{D\mathbf{X}}{Dt} = \mathbf{R}(\mathbf{X}) + \mathbf{D}(\mathbf{X}) + \boldsymbol{\Phi}(\mathbf{X}) \quad (11)$$

where $D\mathbf{X}/Dt$ represents the material derivative, \mathbf{R} the radiation, \mathbf{D} the vertical diffusion and $\boldsymbol{\Phi}$ chemical processes.

The radiation $\mathbf{R}(\mathbf{X})$ can be either offline or online with the prognostic chemical variables - in particular O_3 . In the off-line mode, greenhouse gases and a zonal-mean climatology of O_3 are given as input to the

radiation. Our ozone climatology is based on Paul et al. [73] and HALOE observations above 1 mb. Thus the radiation process takes the form

$$\mathbf{R}(\mathbf{X}) = \begin{pmatrix} \mathbf{R}(\mu^n, \overline{\chi^c}) \\ \mathbf{0} \end{pmatrix}. \quad (12)$$

Since radiation in the troposphere depends on cloud parameters that are diagnostic, and thus not advected, and also depends on temperature that is advected, it is desirable to compute radiation before advection in order to avoid any mismatch in the fields required as input. The radiation update thus operates on the initial state \mathbf{X}^n to create an intermediate state \mathbf{X}_R^* of the form

$$\mathbf{X}_R^* = \begin{pmatrix} \mu_R^* \\ \chi_R^* \end{pmatrix} = \mathbf{X}^n + \Delta t \mathbf{R}(\mathbf{X}^n) = \begin{pmatrix} \mu^n + \Delta t \mathbf{R}(\mu^n, \overline{\chi^c}) \\ \chi^n \end{pmatrix} \quad (13)$$

395 In a fully coupled ozone-radiation configuration that we will consider in Part II of this document, the
396 radiation process then takes the form $\mathbf{R} = \mathbf{R}(\mu^n, \chi_{\text{O}_3}^n)$.

After radiation, advection is processed on both meteorological and chemical variables using \mathbf{X}_R^* as the initial state. Without loss of generality, in a semi-Lagrangian scheme we can write the advection update as,

$$\mathbf{X}_A^* = \begin{pmatrix} \mu_A^* \\ \chi_A^* \end{pmatrix} = \begin{pmatrix} \mu_R^*(\mathbf{x} - \alpha \Delta t) \\ \chi_R^*(\mathbf{x} - \alpha \Delta t) \end{pmatrix}, \quad (14)$$

where \mathbf{x} is the spatial coordinate and α the upstream displacement along the trajectory. The next process to consider is the vertical diffusion $\mathbf{D}(\mathbf{X})$ that is applied on both meteorological and chemical state variables. The resulting update has the form

$$\mathbf{X}_D^* = \begin{pmatrix} \mu_D^* \\ \chi_D^* \end{pmatrix} = \begin{pmatrix} \mu_A^* + \Delta t \mathbf{D}_K(\mu_A^*) \\ \chi_A^* + \Delta t \mathbf{D}_K(\chi_A^*) \end{pmatrix}, \quad (15)$$

using diffusion coefficients K computed from meteorological fields that are common to both meteorological and chemical variables. Finally, the coupled state is updated for the chemical processes,

$$\mathbf{X}^{n+1} = \mathbf{X}_\Phi^* = \begin{pmatrix} \mu_\Phi^* \\ \chi_\Phi^* \end{pmatrix} = \begin{pmatrix} \mu_D^* \\ \chi_D^* + (\mathbf{I} - \Delta t \tilde{\mathbf{J}}_\mu)^{-1} \Delta t \tilde{\mathbf{\Phi}}_\mu(\chi_D^*) \end{pmatrix}, \quad (16)$$

with a resulting state \mathbf{X}^{n+1} . Here in Equation 16, the dependence on μ is actually (T, p) , temperature and pressure. We also use the tilde $\widetilde{(\quad)}$ to emphasize that the Jacobian and chemistry production and loss terms are evaluated in terms of mixing ratio and not in terms of the number density as in Equation 9.

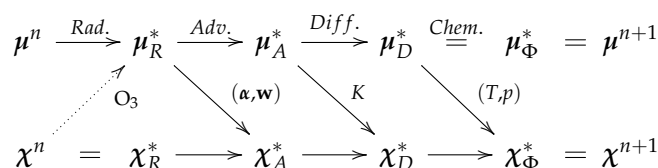


Figure 5. Sequence of processes in the coupled model. Horizontal arrows represents the different process updates as in Equations (13–16). The slanted solid arrows represents the exchange of information from meteorological derived fields to the chemistry and the slanted dot arrow from chemistry to meteorology in ozone-radiation coupling.

Figure 5 displays the sequence of updates of the coupled (augmented) model state and which information is passed from meteorological to chemical modules (up and down arrows). The equal sign indicates that there are no changes and the horizontal arrows indicate changes due to a specific process update. To simplify, let us first discuss the case where there is no ozone-radiation coupling, i.e. let us ignore for now the dotted upward arrow.

First, infrared radiation does not change the chemical concentrations but does change the temperature. Then, the advection of chemical (prognostic) variables requires information about the displacement of the upstream point, α , and the interpolation weights, \mathbf{w} , that are computed from the wind and the position of the upstream point. Next, applying the vertical diffusion on chemical variables requires sharing the diffusion coefficients, K , that are computed from the meteorology. Finally, chemistry requires information about temperature and pressure, but does not change the meteorological variables. When this last update is completed, the state at time t^{n+1} is produced.

In a modular implementation, all processes that involve changes in chemical concentrations (in practice, with the exception of advection) can be included in a chemical module. The computation of the changes in chemical concentrations requires exchange of information through a chemical interface. For example, if we duplicate and include the vertical diffusion routine in the chemical module and pass the K coefficients to the chemistry module, the computation of the vertical diffusion of the chemical variables can be done in the chemistry module. Likewise, in principle, the advection of the chemical variables could be performed in the chemistry module if we duplicate the appropriate routines, but in practice it is easier (in terms of code maintenance), to simply pass the chemical concentrations to the advection routine that computes advection to all meteorological and chemical variables at once.

So far, the exchange of information is performed only one way, from meteorology to chemistry. It is then possible and easy to have a meteorology-only configuration separate from a meteorology-chemistry configuration, by simply allowing advection to be performed on an arbitrary number of variables.

The modularity of this approach can be preserved with sequential processing in the case of ozone-radiation interaction. Indeed, after the whole sequence of processes from advection to increasingly faster processes is completed, the prognostic ozone can be passed as the initial condition to the radiation scheme for the next model time step integration (see dotted upward arrow in Figure 5).

Finally, in terms of computational resources, GEM-BACH is about five times slower than GEM (with no chemistry) on a uniform resolution $1.5^\circ \times 1.5^\circ$, i.e. 240×120 grid points, with 81 vertical levels, and running on 16 CPU (MPI 4 nodes, OpenMP 4 CPU). GEM-BACH transport (advection of 57 species) accounts for about 1/4 of the CPU time, the computational of the J -values for about 1/4 of the CPU time, and the Rosenbrock chemical solver about 1/2 of the CPU time.

5. Coupling with meteorological analyses

The distribution of atmospheric constituents is strongly driven by photochemistry, emissions and meteorology. For this reason, chemical models driven by meteorological analyses can, to a certain degree, simulate observed concentrations at their proper time and location. In terms of chemistry they are free model runs, while the constraints arising from observations come only from the meteorological analysis.

Depending on the type of chemical model coupling, there are different ways meteorological analyses can drive the chemistry. We will discuss how this is done for (offline) chemical transport models (CTM) and one way it is done for dynamically coupled meteorology-chemistry models. Next we detail both of these coupling strategies and discuss their properties and their sources of errors. In section 6, we perform a series of experiments where we estimate the accuracy of both coupling methods by evaluating the chemical simulation against observations.

Coupling of a chemical model with meteorological analysis can be accomplished either:

(CTM) With an *offline* chemical transport model (CTM). Meteorological analyses which are usually produced at regular time intervals, e.g. 6 hours, can be linearly interpolated in time to drive an offline CTM at each time step. This is usually done by interpolating the horizontal wind, temperature and surface pressure and diagnosing the vertical motion from the divergence of the horizontal wind. Alternatively, the vertical motion can also be computed from the diabatic heating rate, giving the vertical motion in isentropic coordinate [89,90], or

(MR) With a coupled dynamical meteorology-chemistry model using *meteorological refresh* (MR). In this case, the coupling is achieved by a direct insertion of meteorological analyses at analysis time. As new analyses are available (e.g. each 6 hours), the meteorological variables of the coupled model are reset to the given meteorological analysis values, but in between, the internal dynamics of the coupled model come from the meteorological driver.

CTM coupling has the *advantage* that there is no discontinuity of the meteorological variables at the analysis times. There is a smooth transition of the meteorology from one meteorological analysis time to the next one. However, because of interpolation in time it has the *disadvantage* that meteorology is not dynamically consistent between analyses.

The MR mode has the advantage and disadvantage interchanged compared to those of the CTM mode. It has the *advantage* that during the model time integration between analyses, the meteorology is dynamically consistent. But it has the *disadvantage* that at the analysis time, there is a discontinuity in the meteorological fields, where the jump is a result of the (meteorological) analysis increment.

Table 2 summarizes how meteorology is effectively used in CTM and MR modes.

Table 2. Effective use of meteorology in CTM and MR modes

	CTM	MR
At analysis times	Continuous meteorology	Discontinuous meteorology
Between analysis times	Dynamically inconsistent	Dynamically consistent

The impact of discontinuity in meteorology and dynamical inconsistency is investigated first theoretically, and then numerically in section 6.

From a theoretical perspective, and for either CTM or MR modes, it is important to note that since there is no chemical data assimilation, the chemical concentrations are time-continuous (both at the meteorological analysis time and between analyses). The absence of changes of concentrations immediately before and immediately after a meteorological analysis time t_A , can be written as

$$\chi(t_A^-) = \chi(t_A^+). \quad (17)$$

However, the time derivative of the concentration at the analysis time t_A is given by

$$\left. \frac{d\chi}{dt} \right|_{t_A^+} - \left. \frac{d\chi}{dt} \right|_{t_A^-} = [\mathbf{V}(t_A^+) - \mathbf{V}(t_A^-)] \cdot \nabla \chi(t_A) = \begin{cases} 0 & \text{CTM mode} \\ \Delta \mathbf{V}^A \cdot \nabla \chi(t_A) & \text{MR mode} \end{cases} \quad (18)$$

where ΔV^A is the wind analysis increment (see Appendix D for a derivation). The time derivative of the concentration is continuous in CTM mode but discontinuous in MR mode.

Let us now outline some properties of the concentration error. In principle, the accumulation of concentration error can be decomposed into two parts: 1- the accumulation of error between the (meteorological) analyses, and 2 - an error at the (meteorological) analysis time. However, since the concentration is time-continuous at analysis time (Equation A9), and since the true concentrations should also be continuous, we conclude that the concentration error is continuous at the meteorological analysis time (and of course also between analyses). Thus, in both CTM and MR modes there is no jump in the concentration error at the (meteorological) analysis time. Also, since the meteorological analysis increment is the same in both CTM and MR experiments, the concentration correction (which can be viewed as an unobserved variable in Equation (5), Part II) should also be the same, provided that the error statistics are the same. We thus conclude that any change in concentration error between CTM or MR modes depends essentially on the error in transport between the meteorological analysis times.

We will present in the following section a comparison of experiments using the CTM and MR modes. However, we can already speculate that the use of linearly interpolated winds (as in CTM mode) would create larger transport (concentration) errors than would a dynamically evolving wind field from a coupled meteorology-chemistry model. Thus, we anticipate that concentration errors in MR mode will be smaller than in a CTM mode.

6. Comparison between CTM and coupled meteorology-chemistry model

Several experiments were carried out in order to quantify the different sources of errors between GEM-BACH in MR mode and the BASCOE CTM. All MR experiments were performed at $1.5^\circ \times 1.5^\circ$, i.e. 240×120 grid points, with 80 levels (27 levels are in the stratosphere) and a 45 minute timestep as described in section 3.1. In the case of the CTM experiments the same horizontal and vertical resolution was used but with a timestep of 15 minutes because its flux-form semi-Lagrangian requires satisfying the Courant-Friedrichs-Lewy condition in the meridional direction. Meteorological analyses were obtained from the Canadian 3D-Var [59] and 4D-Var [60] assimilation systems using, in both cases, the same type of observations (i.e. aircrafts, radiosondes, atmospheric motion vectors, TOVS, GEOS and profiler observations). The most significant difference between the two assimilating systems arises from the capability to use considerably more observations in 4D-Var than in 3D-Var. The meteorological error statistics used are described in [91]. All experiments were evaluated over a period of 12 days in late summer 2003.

Figure 6 shows the results of an ozone simulation for CTM and MR modes using different meteorological analyses. The comparison is made against limb sounding ozone observations from the Envisat/MIPAS instrument. The solid lines depict the mean difference, and the dashed curves the standard deviation. The dashed curves are plotted symmetrically with respect to the zero error (vertical solid black line), simply to illustrate the range of $\pm\sigma$ random errors. Also note that all the errors are normalized by the observed values, so that the errors are expressed as a percentage. The differences are computed from interpolating the model at the observation location, and at the time the observation was made. We emphasize that the chemistry model is the same in all experiments, and the results differ only due to the meteorological analysis and its coupling to the chemistry transport. The red and grey curves are results from using MR (meteorological refresh) mode using the Canadian Meteorological Center (CMC) 3D-Var and 4D-Var meteorological analysis respectively, while the green curves are results based on the CTM mode using 3D-Var analysis.

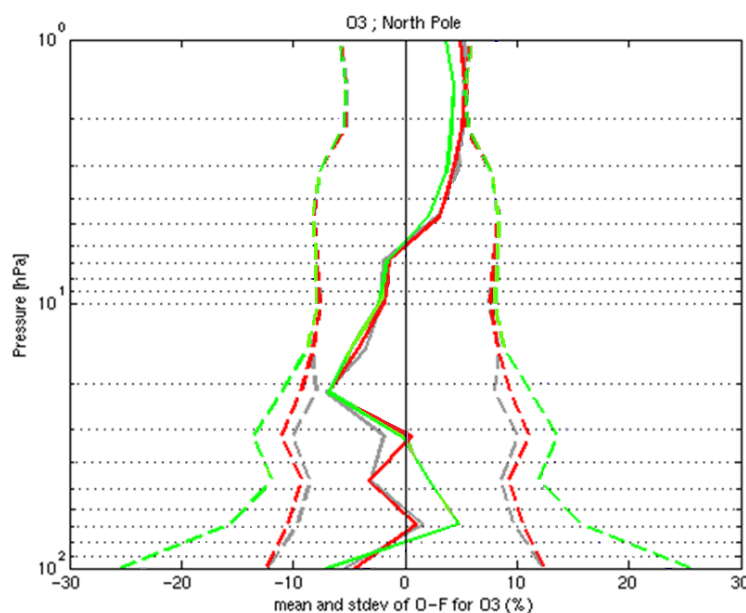


Figure 6. CTM coupling vs MR. Solid curves are mean observation-minus-model differences of O_3 , and dashed curves are error standard deviations. The grey curves correspond to the MR mode using CMC 4D-Var meteorological analyses, the red curves correspond to the 3D-Var meteorological analyses. The green curves correspond to the CTM mode of coupling using the CMC 3D-Var analyses.

First, we draw the reader's attention to the error standard deviation (i.e. dashed curves). We note that between 100 hPa and 20 hPa where the photochemical time scale is of the order of several months (i.e. transport is dominant), the standard deviation is significantly larger with the CTM mode and reaches

twice the MR values at 100 hPa. The difference between green and green curves is only due to the mode of coupling, CTM vs MR.

In terms of the random error (or standard deviation), there is little difference between using 3D-Var and 4D-Var meteorological analyses. The main difference arises from whether the MR mode or CTM mode is used. This indicates that the dynamical inconsistency in the time integration window of 6 hours is the main source of random error, while using different analyses is of secondary importance.

Also, similar conclusions can be drawn for the systematic error (solid curves), where we observe that the main difference in error arises from using either MR or CTM mode of coupling rather than using different meteorological analyses (either 3D- or 4D-Var).

Above 20 hPa, where the photochemical time scale is shorter and transport plays a negligible role with respect to photochemistry, there is no difference in error standard deviation but only a slight difference in systematic error, probably due to differences in mean temperatures between the different modes and different meteorological analyses.

These results clearly indicate that despite the jump in the wind field at the analysis refresh time, the integration consistency which arises in coupling with MR gives a superior chemistry simulation compared to CTM coupling. We conclude that for chemical data assimilation, this implies that the model error due to transport is smaller for coupled models in MR mode compared to offline models in CTM mode.

7. Evaluation of GEM-BACH driven in meteorological refresh (MR) mode

7.1. MIPAS and HALOE measurements

The MIPAS instrument on-board the Envisat satellite is a limb sounder which uses a Fourier transform spectrometer for the detection of emission spectra in the middle and upper atmosphere [5,7]. It observes a wide spectral interval throughout the mid-infrared with high spectral resolution, which permits retrievals of pressure in addition to temperature and volume mixing ratio (VMR) of different gases. The instrument provides about 1,000 profiles per day (day and night) with a global spatial coverage. The operational ESA retrievals v4.61 that we used here do not use any *a priori* and thus can be considered as "pure observations". The typical root-mean-square-error (RMSE) observation error of MIPAS is about 2° K for temperature [92], 10% VMR error for O₃ [93], 20% VMR error for H₂O, CH₄ and N₂O [94,95]. Other species such HNO₃ and NO₂ have a large relative error that varies considerably with altitude (although with a minimum error of 10% at 22 km for HNO₃ and at 40 km for NO₂) [96,97]) and were used in this comparison.

The HALOE instrument on-board the UARS satellite is a solar occultation instrument which employs a broadband radiometer, and a gas correlation technique specifically to infer aerosol extinction [98]. Each HALOE radiometric profile is divided by the exo-atmospheric signal thus giving a direct measurement of the atmospheric transmission for each channel, and retrieves temperature and mixing ratio of a number of species. The horizontal coverage is limited to two latitudes on a given day, one at sunrise and the other at sunset. These sun occultation latitudes change gradually over a period of 45 days, as the UARS satellite is on an inclined orbit and undergoes precession. The whole latitudinal coverage is quite complicated but ranges from $\sim 45^\circ$ in one hemisphere to $\sim 80^\circ$ in the other hemisphere. Each 45 days the hemispheric coverage is inverted through a yaw maneuver of the satellite. The HALOE retrieval of atmospheric constituents is a modified "onion peel" algorithm with no a priori information. The main source of error arises from the absence of pressure measurements. Because of the pointing uncertainty, there is a need to perform a registration of profiles with altitude and pressure, which is done by referencing a meteorological analysis that contains errors [4]. HALOE retrieval V19 used in this study is considered an excellent verification dataset with errors less than 10% for ozone, temperature and H_2O [98–100] and 15% for CH_4 [101].

7.2. GEM-BACH evaluation against satellite observations

7.2.1. Temperature

Temperature is important for the chemistry and for the thermal-wind component of the transport. Figure 7 shows the difference between temperature observations and GEM-BACH driven in MR mode (e.g. positive differences arise when the observed values are larger than the modeled values). Results using MIPAS are displayed in the left panel and HALOE in the right panel. The statistics (mean and standard deviation) use model values interpolated to the proper time and location of the individual observations. The verification results indicate a good agreement for temperatures below 10 hPa and a relatively warm bias above. Since the warm bias between 0.4–10 hPa is similar for both MIPAS and HALOE, we conclude that the bias is due to the model or the meteorological analysis that drives GEM-BACH. Also, we should note that for this two-month period (August 1st to September 30, 2003), the horizontal coverage of the two instruments is not the same. HALOE is limited to the band 40°S to 70°N for this time period.

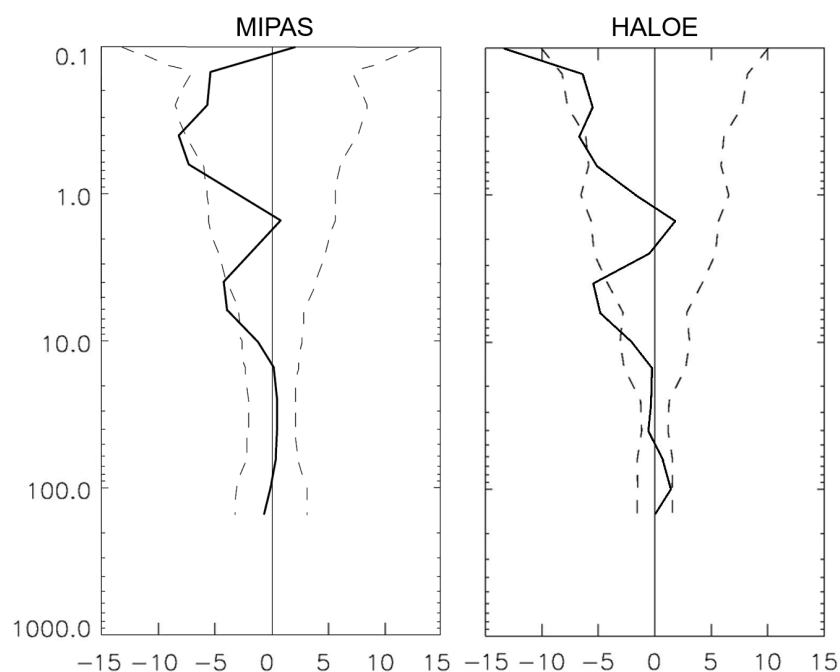


Figure 7. Temporally (August–September 2003) and globally averaged temperature differences between MIPAS and GEM-BACH (left pane) and HALOE and GEM-BACH (right panel) as a function of height (in hPa). The solid lines are the mean difference and the symmetric dashed curves are the standard deviation. The abscissa is in degrees K.

The agreement in temperatures below 10 hPa indicates that MIPAS temperatures are likely to be in agreement with radiosonde temperatures assimilated in GEM-BACH. Indeed, radiosondes measure temperature up to 30 hPa (in the tropics), but their effect on meteorological analyses can be observed up to about 10 hPa. Since radiosonde temperatures provide a strong constraint on meteorological analyses, they have a (significant) impact on GEM-BACH in the MR mode. Thus, the agreement with MIPAS temperatures below 10 hPa, as seen Figure 7, is an indication of a agreement with radiosonde temperatures. Lastly, since we are specifically interested in temperatures over the polar region for heterogeneous chemistry, Figure S7 (Supplementary Material) shows good agreement over the South Pole region (between 70°S and 90°S) during the August–September time period (important for the onset of ozone hole events).

7.2.2. Methane and nitrous oxide

Continuing our assessment of meteorology, evaluation of the distribution of long-lived species, in particular CH₄ and N₂O, can provide information about the quality of the wind fields. The evaluation of CH₄ against MIPAS and HALOE observations is presented in Figure 8. It shows that the model CH₄ is in good agreement with MIPAS observations across the entire stratosphere.

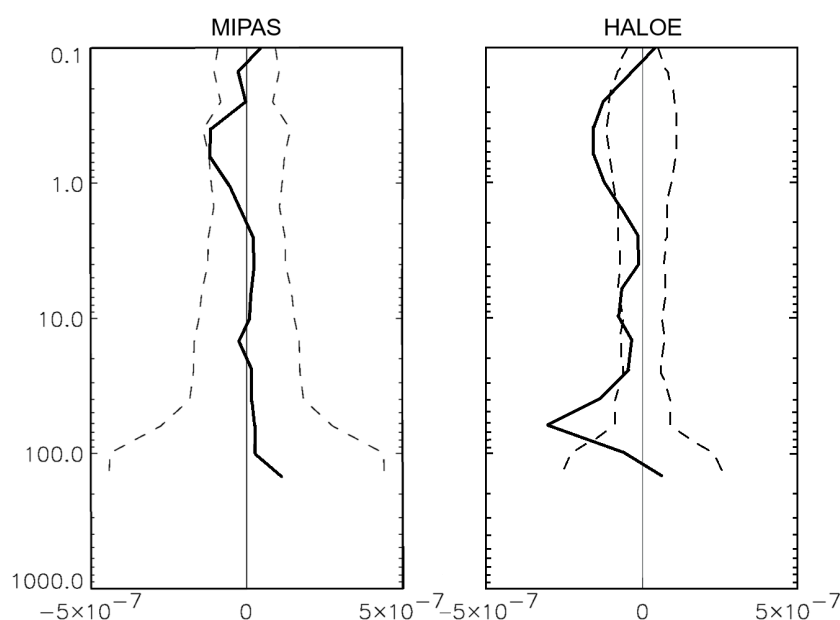


Figure 8. Temporally (August–September 2003) and globally averaged differences of satellite measurements and GEM-BACH modeled CH_4 . Otherwise same as in Figure 7.

Also, a remarkable agreement with MIPAS measurements of N_2O is observed (see Figure S11 in Supplementary Material). These results indicate that the wind fields produced by the meteorological analysis (in MR mode) are of good quality in the stratosphere. However, the comparison with HALOE CH_4 measurements shows non-negligible biases both in the lower and upper stratosphere, but the standard deviation is small, indicating that the spatial patterns in the modeled distribution of CH_4 remain close to the observations.

The fact that accurate winds can be obtained in the stratosphere deserves some attention. We recall that GEM-BACH is driven in MR mode. The meteorological analyses are affected by wind observations only from the troposphere. In the stratosphere, temperature-sensitive radiance observations are the main source of observations. Although satellite radiance observations often have an offset and may result in temperatures being inaccurate (even after the radiance bias correction), we can argue that the horizontal distribution of radiances is well-captured, and consequently the horizontal temperature gradient is well represented. It is known that for the most part, on synoptic time-scales, the stratosphere is in geostrophic balance (and, on large scales, in gradient-wind balance) as discussed in Section 2.2. Thus, we argue based on the thermal-wind relation 3, that the vertical shear of the geostrophic wind in the stratosphere is also well captured since the horizontal gradient of temperatures is reasonably captured by the stratospheric meteorological analyses. The tropospheric winds are also well represented in tropospheric meteorological analysis. Thus, using these winds as the lower boundary condition in the thermal-wind Equation 3, we can

deduce the 3D-distribution of the geostrophic wind in the whole stratosphere. This makes the point that the stratospheric winds are well-represented. Lastly, since the wind field and tracers are closely related as a result of shear flow balanced by stirring and mixing, as discussed in 2.3, we can thus understand that the distribution of long-lived species is also well captured throughout the stratosphere with a coupled model driven in MR mode.

7.2.3. Ozone and water vapour

Important meteorological-chemical interaction arises with gases such as O_3 and H_2O . Global averages of O_3 differences for the same time period are presented Figure 9. We observe a significant model ozone deficit in the upper stratosphere with a maximum deficit of about 15% at 0.7 hPa. This can be explained by the model warm bias at these altitudes and the negative correlation between temperature and ozone, as explained in section 2.1 and with Equation 2. The model ozone deficit in the upper stratosphere may also be partly due the severe overabundance of model NO_2 in the upper stratosphere (see Figure S8 in Supplementary Material), since nitrogen dioxide, NO_2 , catalytically destroys ozone. The model's overestimation of NO_2 is also supported by the comparison of GEM-BACH against FTIR spectrometer measurements at Eureka [102] (see also section 7.3). A better agreement between GEM-BACH and HALOE in terms of O_3 is observed from 2 to 10 hPa, and with overestimation below 10 hPa. This positive bias of GEM-BACH is also seen when we compare the model against ozone sondes (displayed in Figure S9, Supplementary Material). The above considerations indicates that around 30 hPa GEM-BACH O_3 concentrations are too high and that HALOE observations are more accurate than MIPAS ESA retrievals.

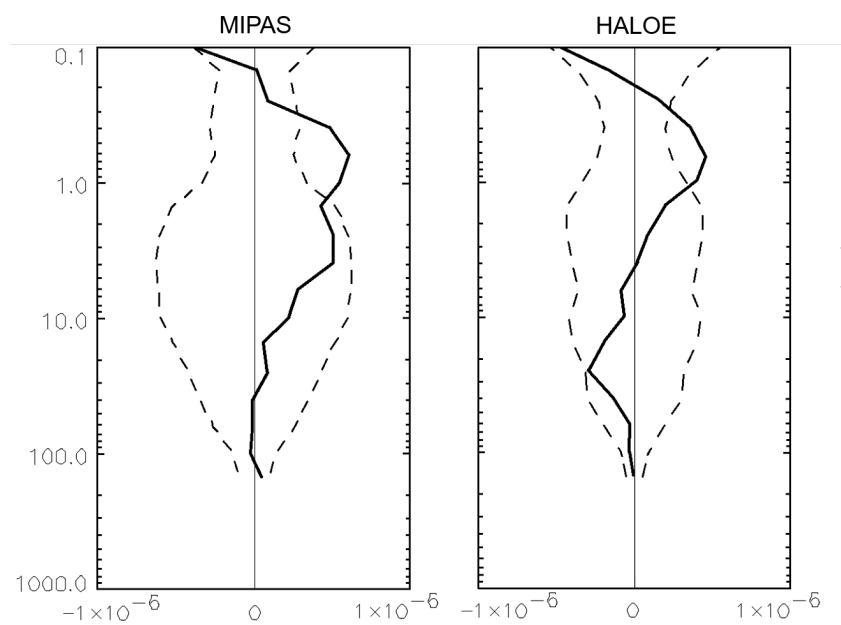


Figure 9. Temporally (August-September 2003) and globally averaged differences in O₃ between, MIPAS versus GEM-BACH (left panel) and HALOE versus GEM-BACH (right panel) as function of height (in hPa). The abscissa is in VMR. Otherwise same as in Figure 7.

Water vapour plays an important role in the ozone budget at the stratopause. It has an important radiative impact in the lower stratosphere/tropopause region. A comparison of GEM-BACH H₂O against MIPAS and HALOE profiles is presented in Figure 10. A good of agreement with MIPAS data throughout the stratosphere as well as a model overestimation near the model top are evident.

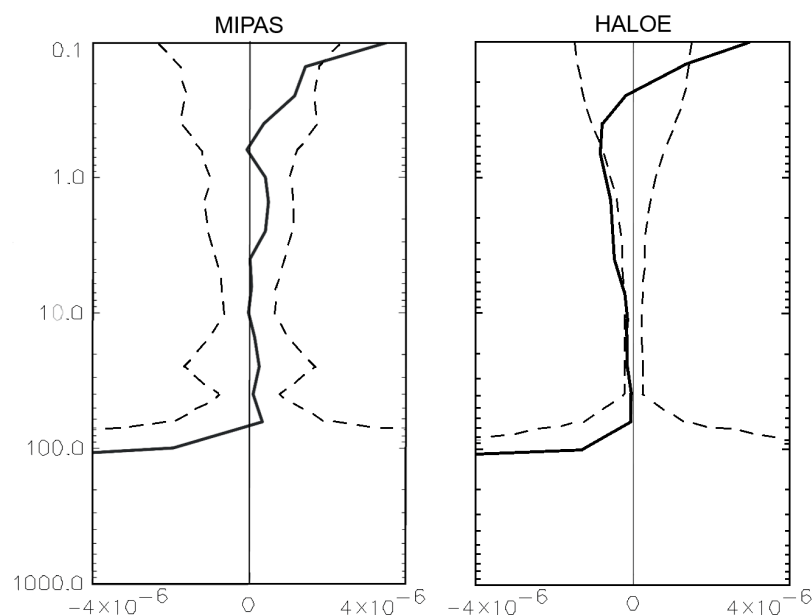


Figure 10. Temporally (August-September 2003) and globally averaged concentrations H_2O . Otherwise same as in Figure 7.

We note, that compared with HALOE data, there is a gradual increase in the H_2O bias with height, indicating a positive model bias which grows gradually with height across the stratosphere. Closer to the tropopause, we observe a significant model underestimation compared to both MIPAS and HALOE data. Since the retrieval error is important and the variability of H_2O is very large, a definitive conclusion would require a closer investigation, which we have not carried out here. In fact, since there is a sharp transition in H_2O at the tropopause and because the height varies considerably between the tropics and the polar regions, the global average is simply not a good comparison statistic.

7.3. GEM-BACH evaluation against ground-based total column measurements

An evaluation of the stratospheric column of GEM-BACH was made against the Network for the Detection of Atmospheric Composition Change (NDACC) Bruker 125HR Fourier-Transform InfraRed (FTIR) spectrometer at Eureka (Nunavut, Canada (80.05°N , 86.42°W)). The comparison was carried out during the International Polar Year (IPY), from March 1st 2007 to February 28th 2009 and the data are publicly available on the SPARC-IPY web site [103].

The FTIR instrument, retrieval methods and measurements during this time are described in depth in Batchelor et al. [104,105]. While an additional comparison between this FTIR and GEM-BACH and other models for the NO_y budget has been published by Lindenmaier et al. [102], it is valuable to provide an

640 example of how GEM-BACH compares with ground-based measurements as part of this discussion, and
641 more so for O₃, HCl and CH₄ which were not examined in [102].

642 Comparisons between the FTIR stratospheric partial columns measured at Eureka for six chemical
643 species during 2007 are shown in Figure 11. Here the GEM-BACH model is refreshed with Canadian
644 meteorological 3D-Var-FGAT (First Guess At correct Time) analyses every 12 hours. The configuration of
645 GEM-BACH is identical to that described in section 3 except that the surface area density for the PSC's has
646 been reduced to provide a better agreement with ozone observations in polar regions.

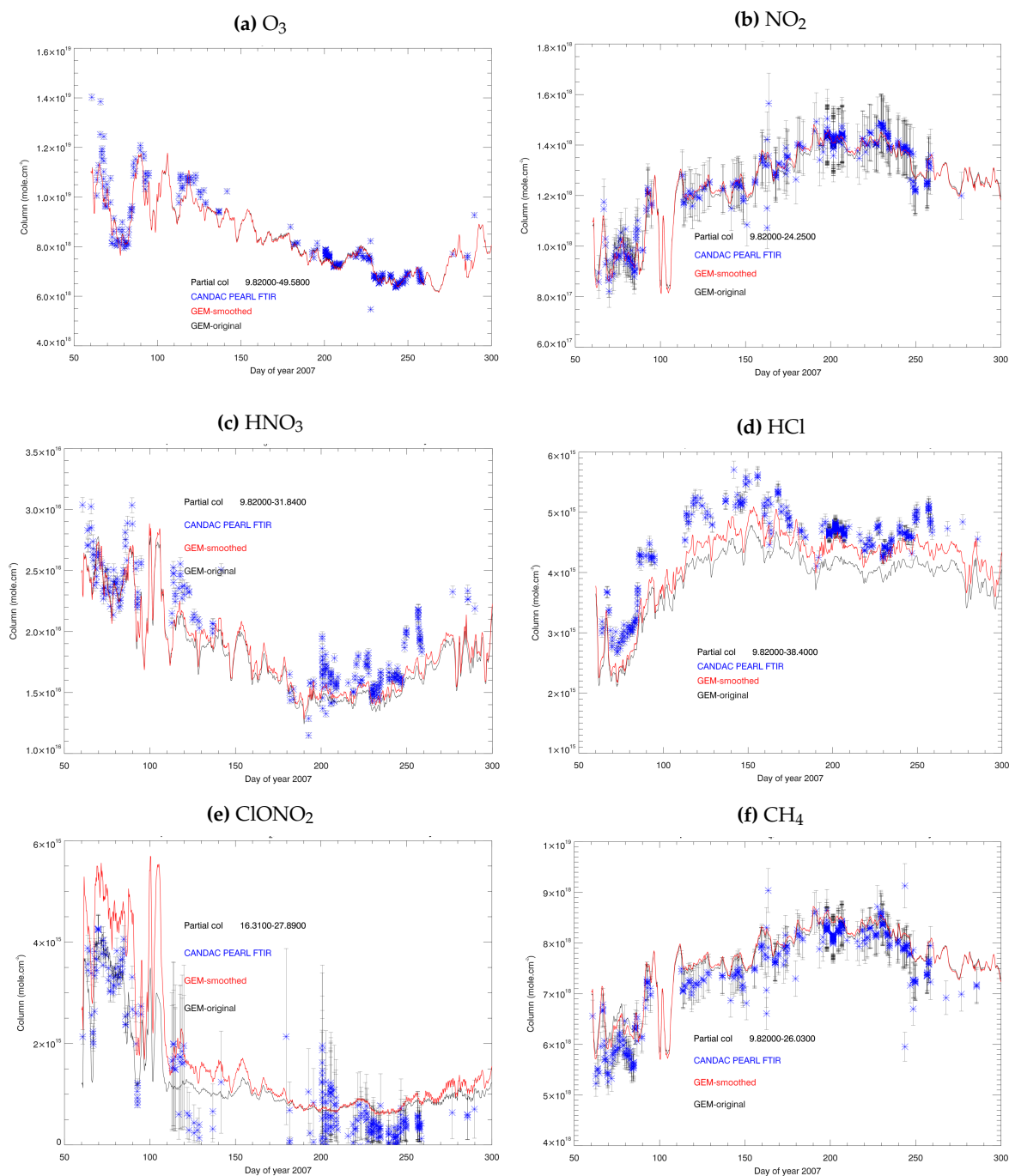


Figure 11. Lower stratospheric partial columns of O₃, NO₂, HNO₃, HCl, ClONO₂, and CH₄ (left to right, top to bottom) as observed by the FTIR spectrometer at Eureka (blue stars and black error bars) compared with the same partial columns determined from the GEM-BACH simulation before (black line) and after (red line) vertical smoothing based on averaging kernels and a priori of the FTIR retrieval. The pressure bounds for the partial column differ for each species (see plot inset; units are in hPa) to select the vertical range where the sensitivity of the FTIR is > 0.5.

As described in [104,105], the vertical resolution of the FTIR measurements is limited, and in some parts of the atmosphere the a priori contributes significantly to the column. To account for this and provide a clean comparison, the higher-resolution GEM profile χ_m is smoothed with the FTIR a priori χ_a and averaging kernel \mathbf{A} , to provide a smoothed profile χ_s as defined in [106],

$$\chi_s = \chi_a + \mathbf{A}(\chi_m - \chi_a). \quad (19)$$

The column is determined from the smoothed profile, with the partial column bounded between 9.8 hPa (corresponding to approximately the bottom of the stratosphere) and the maximum altitude where data contributes more than the a priori (sensitivity >0.5) to the FTIR retrieval. The argument to use Equation 19 can be understood from the fact that if we replace χ_m by the true concentration χ , we get the standard expression for a retrieved profile using the averaging kernel \mathbf{A} . Then, with the ansatz that GEM-BACH provides an ideal high resolution profile, if we substitute it for the truth, we then get a smoothed or equivalent "retrieved" profile [106] that we can compare with the FTIR retrieval.

Observations at Eureka provide a usefully challenging test case for modeling, with the dynamic polar vortex allowing air inside, through the edge, and outside of the vortex to be sampled overhead. Figure 11 demonstrates how well GEM-BACH captures this dynamical variability. Between day 65 and 85 of the SPARC-IPY campaign, the FTIR sampled the air mass inside the polar vortex, as seen in the perturbed profile across all the gases. The 2006/2007 polar winter was characterized by a strong, cold polar vortex with significant amounts of ozone depletion [107,108]. This is well captured in the model, with ozone (panel (a)) tracking the FTIR columns extremely closely, both inside and outside the vortex. The day-to-day dynamic and seasonal variability is captured throughout the year across all gases, suggesting that both meteorological and radiation processes are being captured well. As described in [102] there are some consistent offsets seen between the model and data in the chlorine reservoir species HCl and ClONO₂, and in HNO₃ (though the latter matches well within the 2007 vortex, GEM-BACH is typically 10% lower than observed throughout the rest of the comparison period [106]). These differences are likely due to not including all of the chlorine sources (CFCs), as well as limitations in the PSC treatment, which is tuned to Antarctic conditions and does not include type 1b liquid PSC particles, which play a bigger role in the Arctic [106].

Methane (CH₄) is an important greenhouse gas, and several recent studies have focused on better understanding the contribution of the stratosphere on the methane column [109,110]. Figure 11 panel (f) shows a seasonal bias in the modelled stratospheric CH₄, with excellent agreement in the summer and a

high bias in the spring and fall. A similar overestimation of CH₄ at high northern latitudes is observed and the cause remains a subject of investigation.

8. Discussion on the use of lower resolution

It has been argued that the tracer distribution is primarily controlled by the large-scale low-frequency component of the flow [35] and thus, a lower resolution meteorology could be used in a chemical transport model, and yet produce realistic simulations. A similar argument exists for meteorological data assimilation, where lower resolution analysis increments produced in a 4D-Var scheme (i.e. incremental 4D-Var) are able to create realistic small scale structures over time through the atmospheric model [111,112]. The arguments presented for both tracer-wind transport and the incremental 4D-Var are based on models that are dominated by an enstrophy cascade with a spectra k^{-3} spectrum, where k is the wavenumber. Large-scale lower-resolution atmospheric and barotropic vorticity models have such behavior - the sources of energy injected at low wavenumbers cascade down to higher wavenumbers. However, in the stratosphere with high resolution meteorological models, the energy spectra evolve from steep spectra, $\propto k^{-3}$, to a shallow spectra as the height increases [113] resulting from an inverse energy cascade $\propto k^{-5/3}$ at high wave numbers. We thus expect that GEM-BACH has a similar behavior.

The chemical tracer field has what is called a scalar variance spectra, that has in theory a slope lying between -1 for enstrophy-cascade dynamics to -5/3 for the inverse energy cascade dynamics [114]. However because of mixing barriers and trapping by persistent vortices, it has been argued that the scalar spectral slope can be as steep as -2 in those cases [115]. However, in general, stratospheric observations indicate that slopes of -5/3 in the scalar variance are usually obtained [116,117].

In the context of tracer-wind transport, the argument that low resolution winds can reproduce the small scale structure of tracer fields has been challenged by Bartello [114]. He pointed out that lower resolution models dominated by enstrophy-cascade dynamics can reproduce accurately some fine structure of the tracer field [114,118] using a relatively coarse wind field. However, higher resolution models, with an inverse energy cascade at smaller scales, create fictitious small scale structures in the tracer field when coarse resolution winds are used [114].

These results are of direct relevance to coupled stratospheric chemistry-meteorology modeling and data assimilation. In the stratosphere, where the inverse energy cascade is important, the use of lower resolution analysis increments, e.g. incremental 4D-Var, is expected to result in a loss of information in the stratospheric meteorological analysis. Furthermore, the chemical tracer fields driven by lower resolution analysis increments would also lose accuracy in small scale structures. For these reasons, we argue that for

703 stratospheric models such as GEM-BACH, we should generate analysis increments at the same resolution
704 as the meteorological model, and also drive the chemistry at the same resolution as the meteorological
705 model, so as not to introduce small-scale errors in both meteorology and chemical tracer fields.

706 Bartello [114] also noted that the temporal resolution of the advecting velocity would have a time-scale
707 $\propto k^{-2/3}$ and thus an increase in spatial resolution requires a corresponding increase in temporal sampling.
708 Linear time interpolation used in CTM's would then be detrimental, that has been clearly identified in
709 section 6.

710 To illustrate our discussion in regard to resolution, we have chosen an ozone depletion event and
711 conducted a few experiments over the period August-October 2003. Figure 12 panel (a) shows the total
712 column ozone measurements from the TOMS instrument on September 30, 2003. Typical to such events,
713 we note there is a wide range of total ozone amounts (and thus of ozone concentration values) and sharp
714 gradients along the vortex edge. First, we have conducted a 3D-Var meteorological assimilation with
715 GEM at $1.5^\circ \times 1.5^\circ$ resolution producing analysis increments at the same resolution, and driving the
716 coupled model GEM-BACH in the MR mode also at the same resolution. The results of this pure chemical
717 simulation are presented in panel (b) of Figure 12. We observe a remarkably accurate simulation of the
718 ozone depletion event, with accurate vortex values, sharp gradients along the vortex edge and reasonably
719 well-reproduced mid-latitude surf-zone values. Tropical values (see Figure S12 in Supplementary Material)
720 are lower than observed (we know from section 7.2.3 that GEM-BACH model has an ozone deficit problem).
721 Nevertheless this represents a major accomplishment, accounting for the fact that there is no chemical
722 assimilation in this run.

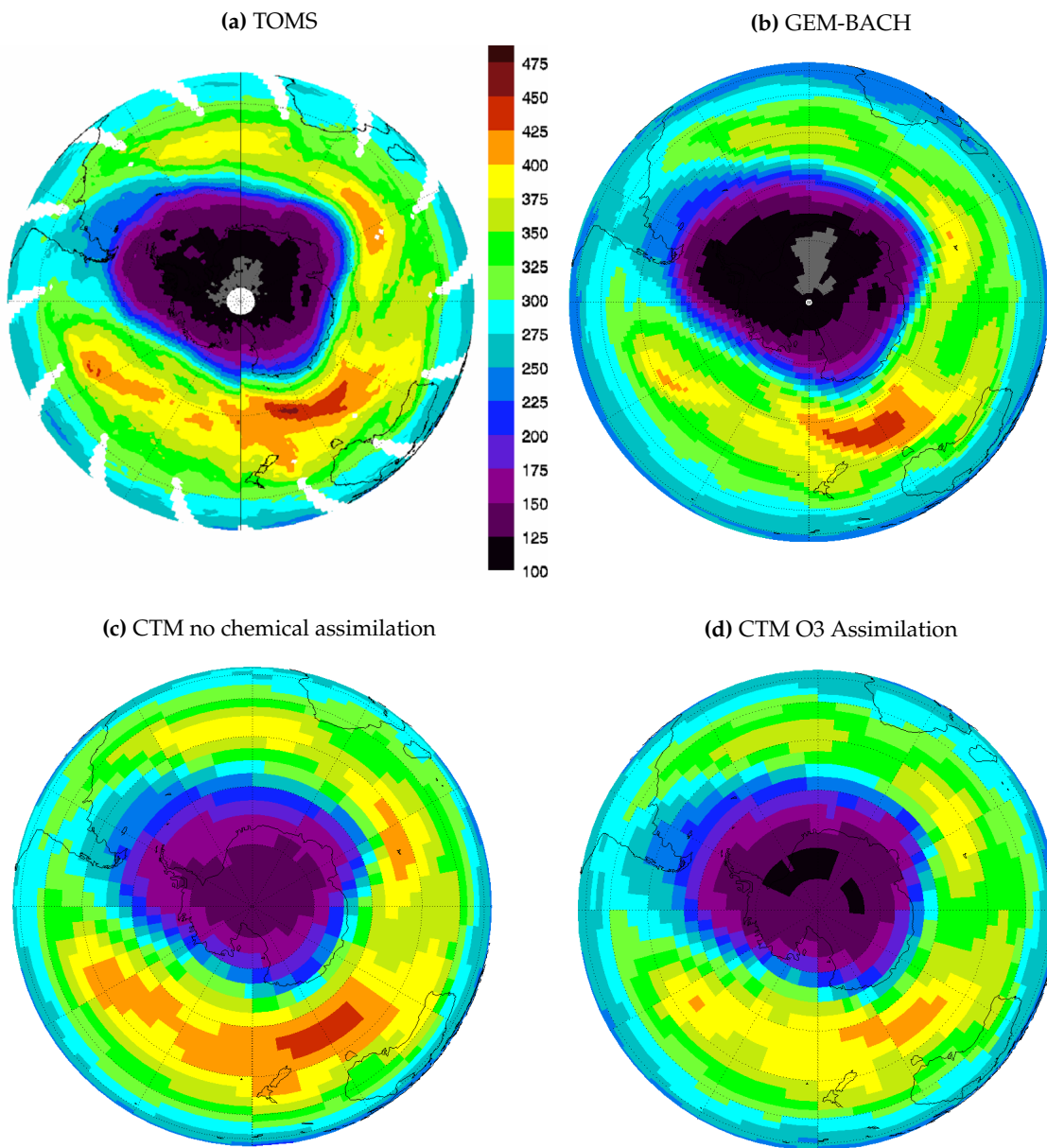


Figure 12. Total column ozone (DU) for September 30th 2003. Panel (a) Observations from TOMS (v7). Panel (b) GEM-BACH refreshed with the Canadian 3D-Var analysis. Panel (c) CTM in low resolution mode ($3.75^\circ \times 5^\circ$). Panel (d) BASCOE 4D-Var assimilation of ozone MIPAS (ESA) observations. Grey areas represent pixels where the ozone column is smaller than 100 DU.

723 We now compare the BASCOE CTM (panel c) and 4D-Var chemical data assimilation (panel d), as
 724 done operationally at BIRA, using the operational ECMWF meteorological analysis. Since 4D-Var chemical
 725 assimilation is costly, the model and assimilation are performed at a lower resolution, in the case here both
 726 at $3.75^\circ \times 5^\circ$. As in GEM-BACH, heterogeneous chemistry is simulated using prescribed climatological

SAD values (see section 3.2). The CTM simulation with the coarser-grained model overestimates both the vortex and mid-latitude surf-zone values and has weak gradients at the vortex edge. Thus, it appears that lower resolution winds driving a chemical model at the same resolution cannot reproduce the sharp gradients (i.e. small scale structures in the chemical field) at the vortex edge. Although this result is simply an illustration, it does not support the claim that the large-scale, low-frequency component of the flow controls the tracer distribution. It is important to note that both the BASCOE CTM and GEM-BACH have no horizontal diffusion that could smooth horizontal gradients. Any horizontal gradient or lack thereof is a result of the driving winds and underlying cascade regime.

Next, a 4D-Var assimilation of ozone observation from MIPAS was conducted and the result is presented in panel (d). We note lower ozone values in the polar vortex but the horizontal extent of low values is not as large as in the case of BASCOE. We also observe a weakening of the concentrations outside the polar vortex. This is apparently an effect of the error covariances and the impact of observations near the vortex edge that tend to mix values in and out of the vortex, which can be partly alleviated if a more appropriate covariance model is used [119].

9. Summary and conclusions

A fully coupled meteorology-chemistry model, called GEM-BACH, was developed by combining the stratospheric extension of the NWP model GEM with the BASCOE chemical transport model using a chemical interface that preserves time splitting properties while being modular, allowing the system to run with or without chemistry. The increase in computational cost was minimal due to the semi-Lagrangian scheme where the upstream point and interpolation weights are computed only once for all species.

The project started with a very preliminary stratospheric version of the CMC operational meteorological model GEM. The inclusion of a non-orographic gravity wave drag by Hines [43,44] and a k-correlated radiative scheme due to Li and Barker [68] has produced realistic lower stratosphere temperatures over the South Pole for the initiation of PSC chemistry with a realistic simulation of the ozone hole without chemical data assimilation, a rare outcome for a pure simulation (Guy Brasseur, personal communication).

We compared chemical observations with GEM-BACH with the meteorology component replaced by meteorological analysis every 6 hours. This mode of coupling with meteorological analyses was called meteorological refresh (MR) mode, and the accuracy of the simulated chemistry was compared with the standard CTM approach, where an offline chemistry model is driven by meteorological analyses linearly interpolated in time. The results show that the dynamical consistency provided by the coupled

model driven with meteorological analysis refresh (MR), although with an offset created every 6 hours by the meteorological analysis, is much more accurate than a linear interpolation of analyses used to drive an offline CTM. This conclusion was reached irrespectively of the type of meteorological analysis used, whether it came from a 3D-Var 4D-Var assimilation scheme.

The temperature in GEM-BACH, driven in MR mode with the standard meteorological observations showed a fairly good agreement in the lower stratosphere with independent temperature measurements from MIPAS and HALOE. But large and similar biases against MIPAS and HALOE were observed in the middle and upper stratosphere, indicating a warm bias in either GEM or in the standard meteorological temperature data. On the other hand, the quality of the transport, evaluated by comparing the model to observations of long-lived chemical species, showed good quality throughout the stratosphere, both in a global time-averaged mean and in their daily variability, compared with total column ground-based FTIR measurements. However, the model upper stratospheric ozone was underestimated by the BASCOE chemistry, which may be attributable to temperature overestimation or poorly modeled NO_x at these altitudes. Rather good agreement was observed with chemically produced H₂O throughout the stratosphere.

Finally, we add a discussion on the importance of having a meteorological analysis and analysis increment computed at the same resolution as in the coupled model. The GEM-BACH simulation of the ozone hole event of 2003, with the coupled model driven in MR mode, showed particularly good results compared with independent observations, in terms of values inside and outside the vortex, as well as the gradient along the vortex edge. The quality of the 4D-Var ozone assimilation performed with a CTM at much lower resolution did not approach the simulations with GEM-BACH, thus stressing the importance of resolution in obtaining accurate chemical fields.

Author Contributions: Conceptualization, R.M.; methodology, R.M., S.C. and M.C.; software, S.C., M.C., A.K., A.R., J. de G., and J.K.; validation, R.M., S.C., R.B. and M.C.; formal analysis, R.M., J. de G. and S.C.; investigation, S.C., M.C., R.B., A.R., M.R., J. de G. and J.K.; data curation, S.C. and M.R.; writing—original draft preparation, R.M. and S.C.; writing—review and editing, A.K., R.B. and J. de G.; visualization, R.M., S.C., A.R. and J. de G.; supervision, R.M. and S.C.; project administration, R.M.; funding acquisition, R.M.

Funding: This work was funded by the European Space Agency/ESTEC contract No. 18560/04/NL/FF "Coupled Chemistry-Dynamics Data Assimilation" with the Contract Officer Tobias Wehr (ESA/ESTEC). This work was also supported in kind from the Atmospheric Science and Technology Directorate of Environment and Climate Change Canada (ECCC). The Eureka FTIR measurements were made at the Polar Atmospheric Research Laboratory under the CANDAC project led James R. Drummond, and in part by the Canadian Arctic ACE/OSIRIS Validation Campaigns lead by Kaley A. Walker. Funding was also provided by AIF/NSRIT, CFI, CFCAS, CSA, ECCC, GOC-IPY, NSERC,

NSTP, OIT, and ORF. Logistical and operational support was provided by the PEARL Site Manager Pierre Fogal, the CANDAC operators, and the ECCC Weather Station.

Acknowledgments: We wish to thank Saroja Polavarapu for her numerous advice and as the Canadian IPY representative for her help in facilitating the production and storage of the data on the IPY data repository. We wish to thank Kimberly Strong at University of Toronto as the PI of the FTIR measurements at Eureka, who provided access to the measurement data. We wish thank Michel Béland, Director of Climate and Atmospheric Research Directorate and late Keith Puckett Director of the Air Quality Research Division both Environment and Climate Change Canada for their continuous support in making this project a reality. We thank Dominique Fonteyn from the Belgian Institute for Space Aeronomy for the initiation of our fruitful partnership. We thanks Paul Vaillancourt, Paul André Beaulieu, Sylvain Ménard, Mike Neish and Cathy Xie from ECCC, and late John C. McConnell from York University as well as Quentin Errera from BIRA for their help and advice on specific issues. Finally, we are grateful to all the authors for an early review of the manuscript and for the anonymous reviewers.

Conflicts of Interest: The authors declare no conflict of interest. The funders had no role in the design of the study; in the collection, analyses, or interpretation of data; in the writing of the manuscript, or in the decision to publish the results.

Abbreviations

The following abbreviations are used in this manuscript:

BASCOE	Belgian Assimilation System for Chemical ObsErvations
BIRA	Belgian Institute for Space Aeronomy
CMC	Canadian Meteorological Center
CRISTA	CRyogenic Infrared Spectrometers and Telescopes for the Atmosphere
CTM	Chemical Transport Model
ECCC	Environment and Climate Change Canada
ECMWF	European Centre for Medium Range Forecasting
EOS	Earth Observing System
ESA	European Space Agency
FGAT	First Guess At appropriate Time
FTIR	Fourier Transform InfraRed spectrometer
GAW	Global Atmospheric Watch
GCCM	Global Chemistry Circulation Model
GEM	Global Environmental Multiscale
GEM-BACH	GEM Belgian Atmospheric CHemistry
GHG	Greenhouse Gas

GMAO	Global Modeling and Assimilation Office
GOME	Global Ozone Monitoring Experiment
GWD	Gravity Wave Drag
HALOE	HALogen Occultation Experiment
IPY	International Polar Year
IR	Infrared
KPP	Kinetic PreProcessor
LINOZ	LINearized model for OZone
MDPI	Multidisciplinary Digital Publishing Institute
MERRA	Modern-Era Retrospective analysis for Research and Applications
MIPAS	Michelson Interferometer for Passive Atmospheric Sounding
MLS	Microwave Limb Sounder
MR	Meteorological Refresh mode
NASA	National Aeronautics and Space Administration
NAT	Nitric Acid Trihydrate
NDACC	Network for the Detection of Atmospheric Composition Change
NWP	Numerical Weather Prediction
PSC	Polar Stratospheric Cloud
QBO	Quasi-Biennial Oscillation
RMSE	Root Mean Square Error
SAD	Surface Area Densities
SLIMCAT	Single Layer Isentropic Model of Chemistry And Transport
SPARC	Stratosphere-troposphere Processes And their Role in Climate
SSA	Stratospheric Sulfate Aerosols
TOMS	Total Ozone Mapping Spectrometer
TUV	Tropospheric Ultraviolet and Visible model
UARS	Upper Atmosphere Research Satellite
UKMO	United Kingdom Meteorological Office
UV	Ultra-violet
VMR	Volume Mixing Ratio
WMO	World Meteorological Organization
3D-var	Three-dimensional variational method
4D-var	Four-dimensional variational method

810

811 Appendix A. List of chemical reactions

Table A1. Gas phase reactions

$(*) \text{O} + \text{O}_2 \rightarrow \text{O}_3$ $\text{O}^{1\text{D}} + \text{N}_2 \rightarrow \text{N}_2\text{O}$ $\text{O}^{1\text{D}} + \text{O}_3 \rightarrow \text{O} + \text{O} + \text{O}_2$ $\text{O}^{1\text{D}} + \text{CH}_4 \rightarrow \text{CH}_2\text{O} + \text{H}_2$ $\text{O}^{1\text{D}} + \text{N}_2\text{O} \rightarrow \text{NO} + \text{NO}$ $\text{CFC11} + \text{O}^{1\text{D}} \rightarrow 3 \text{Cl} + \text{HF}$ $\text{CFC114} + \text{O}^{1\text{D}} \rightarrow 2 \text{Cl} + 4 \text{HF}$ $\text{HA1211} + \text{O}^{1\text{D}} \rightarrow \text{Br} + \text{Cl} + 2 \text{HF}$ $\text{HCFC22} + \text{OH} \rightarrow \text{Cl} + \text{H}_2\text{O}$ $\text{CH}_3\text{CCl}_3 + \text{OH} \rightarrow 3 \text{Cl} + \text{H}_2\text{O}$ $\text{H} + \text{O}_2 \rightarrow \text{HO}_2$ $\text{OH} + \text{O}_3 \rightarrow \text{HO}_2 + \text{O}_2$ $\text{OH} + \text{OH} \rightarrow \text{H}_2\text{O}_2$ $\text{H} + \text{HO}_2 \rightarrow 2 \text{OH}$ $\text{HO}_2 + \text{OH} \rightarrow \text{H}_2\text{O} + \text{O}_2$ $\text{H}_2\text{O}_2 + \text{O} \rightarrow \text{OH} + \text{HO}_2$ $\text{NO} + \text{HO}_2 \rightarrow \text{NO}_2 + \text{OH}$ $\text{NO} + \text{O} \rightarrow \text{NO}_3 + \text{O}_2$ $\text{NO}_2 + \text{HO}_2 \rightarrow \text{HNO}_4$ $\text{NO}_3 + \text{NO}_2 \rightarrow \text{N}_2\text{O}_5$ $\text{HNO}_4 + \text{OH} \rightarrow \text{H}_2\text{O} + \text{NO}_2 + \text{O}_2$ $\text{NO}_3 + \text{HO}_2 \rightarrow \text{NO}_2 + \text{OH} + \text{O}_2$ $\text{N} + \text{O}_2 \rightarrow \text{N}_2 + \text{O}$ $\text{Cl} + \text{O}_3 \rightarrow \text{ClO} + \text{O}_2$ $\text{Cl} + \text{CH}_2\text{O} \rightarrow \text{HCl} + \text{HCO}$ $\text{Cl} + \text{H}_2\text{O} \rightarrow \text{HCl} + \text{HO}_2$ $\text{Cl} + \text{OCIO} \rightarrow \text{ClO} + \text{ClO}$ $\text{ClO} + \text{O} \rightarrow \text{Cl} + \text{O}_2$ $\text{ClO} + \text{HO}_2 \rightarrow \text{O}_2 + \text{HOCl}$ $\text{ClO} + \text{ClO} \rightarrow \text{Cl} + \text{OCIO}$ $\text{ClO} + \text{ClO} \rightarrow \text{Cl}_2\text{O}_2$ $\text{Cl}_2\text{O}_2 \rightarrow 2 \text{ClO}$ $\text{OCIO} + \text{O} \rightarrow \text{ClO} + \text{O}_2$ $\text{HOCl} + \text{O} \rightarrow \text{ClO} + \text{OH}$ $\text{ClONO}_2 + \text{O} \rightarrow \text{ClO} + \text{NO}_3$ $\text{NO}_2 + \text{Cl} \rightarrow \text{ClNO}_2$ $\text{HCl} + \text{O}^{1\text{D}} \rightarrow \text{OH} + \text{Cl}$ $\text{Br} + \text{HO}_2 \rightarrow \text{HBr} + \text{O}_2$ $\text{BrO} + \text{O} \rightarrow \text{Br} + \text{O}_2$ $\text{BrO} + \text{NO}_2 \rightarrow \text{BrONO}_2$ $\text{BrO} + \text{ClO} \rightarrow \text{BrCl} + \text{O}_2$ $\text{HBr} + \text{OH} \rightarrow \text{Br} + \text{H}_2\text{O}$ $\text{Br}_2 + \text{OH} \rightarrow \text{HOBr} + \text{Br}$ $\text{CO} + \text{OH} \rightarrow \text{H} + \text{CO}_2$ $\text{CH}_2\text{O} + \text{O} \rightarrow \text{HCO} + \text{OH}$ $\text{CH}_3\text{O} + \text{O}_2 \rightarrow \text{CH}_2\text{O} + \text{HO}_2$ $\text{CH}_3\text{O}_2 + \text{NO} \rightarrow \text{CH}_3\text{O} + \text{NO}_2$ $\text{CH}_3\text{OOH} + \text{OH} \rightarrow \text{CH}_3\text{O}_2 + \text{H}_2\text{O}$ $\text{CO} + \text{O} \rightarrow \text{CO}_2$	$(*) \text{O} + \text{O}_3 \rightarrow 2 \text{O}_2$ $\text{O}^{1\text{D}} + \text{O}_2 \rightarrow \text{O} + \text{O}_2$ $\text{O}^{1\text{D}} + \text{H}_2\text{O} \rightarrow 2 \text{OH}$ $\text{O}^{1\text{D}} + \text{CH}_4 \rightarrow \text{CH}_3 + \text{OH}$ $\text{O} + \text{O} \rightarrow \text{O}_2$ $\text{CFC12} + \text{O}^{1\text{D}} \rightarrow 2 \text{Cl} + 2 \text{HF}$ $\text{CFC115} + \text{O}^{1\text{D}} \rightarrow \text{Cl} + 5 \text{HF}$ $\text{HA1301} + \text{O}^{1\text{D}} \rightarrow \text{Br} + 3 \text{HF}$ $\text{CH}_3\text{Cl} + \text{OH} \rightarrow \text{HO}_2 + \text{Cl}$ $\text{CH}_3\text{Br} + \text{OH} \rightarrow \text{Br} + \text{H}_2\text{O}$ $\text{H} + \text{O}_3 \rightarrow \text{OH} + \text{O}_2$ $\text{OH} + \text{O} \rightarrow \text{O}_2 + \text{H}$ $\text{HO}_2 + \text{O} \rightarrow \text{OH} + \text{O}_2$ $\text{H} + \text{HO}_2 \rightarrow \text{H}_2\text{O} + \text{O}$ $\text{HO}_2 + \text{HO}_2 \rightarrow \text{H}_2\text{O}_2 + \text{O}_2$ $\text{H}_2 + \text{O} \rightarrow \text{OH} + \text{H}$ $\text{NO}_2 + \text{O} \rightarrow \text{NO} + \text{O}_2$ $\text{NO}_2 + \text{O}_3 \rightarrow \text{NO}_3 + \text{O}_2$ $\text{NO}_3 + \text{O} \rightarrow \text{O}_2 + \text{NO}_2$ $\text{N}_2\text{O}_5 \rightarrow \text{NO}_2 + \text{NO}_3$ $\text{HNO}_4 \rightarrow \text{HO}_2 + \text{NO}_2$ $\text{NO}_3 + \text{HO}_2 \rightarrow \text{HNO}_3 + \text{O}_2$ $\text{NO} + \text{O} \rightarrow \text{NO}_2 + \text{O}$ $\text{Cl} + \text{H}_2 \rightarrow \text{HCl} + \text{H}$ $\text{Cl} + \text{HO}_2 \rightarrow \text{HCl} + \text{O}_2$ $\text{Cl} + \text{HOCl} \rightarrow \text{Cl}_2 + \text{OH}$ $\text{Cl} + \text{ClOO} \rightarrow \text{Cl}_2 + \text{O}_2$ $\text{ClO} + \text{OH} \rightarrow \text{HO}_2 + \text{Cl}$ $\text{ClO} + \text{NO} \rightarrow \text{NO}_2 + \text{Cl}$ $\text{ClO} + \text{ClO} \rightarrow \text{Cl} + \text{ClOO}$ $\text{ClOO} \rightarrow \text{Cl} + \text{O}_2$ $\text{HCl} + \text{OH} \rightarrow \text{H}_2\text{O} + \text{Cl}$ $\text{OCIO} + \text{OH} \rightarrow \text{HOCl} + \text{O}_2$ $\text{HOCl} + \text{OH} \rightarrow \text{H}_2\text{O} + \text{ClO}$ $\text{ClONO}_2 + \text{OH} \rightarrow \text{HOCl} + \text{NO}_3$ $\text{NO}_3 + \text{Cl} \rightarrow \text{ClO} + \text{NO}_2$ $\text{Cl}_2\text{O}_2 + \text{Cl} \rightarrow \text{Cl}_2 + \text{Cl} + \text{O}_2$ $\text{Br} + \text{CH}_2\text{O} \rightarrow \text{HBr} + \text{HCO}$ $\text{BrO} + \text{HO}_2 \rightarrow \text{HOBr} + \text{O}_2$ $\text{BrO} + \text{ClO} \rightarrow \text{Br} + \text{OCIO}$ $\text{BrO} + \text{BrO} \rightarrow 2 \text{Br} + \text{O}_2$ $\text{HBr} + \text{O} \rightarrow \text{Br} + \text{OH}$ $\text{BrO} + \text{OH} \rightarrow \text{HO}_2 + \text{Br}$ $\text{CH}_4 + \text{OH} \rightarrow \text{CH}_3 + \text{H}_2\text{O}$ $\text{HCO} + \text{O}_2 \rightarrow \text{CO} + \text{HO}_2$ $\text{CH}_3\text{O}_2 + \text{NO} \rightarrow \text{CH}_3\text{O} + \text{NO}_2$ $\text{CH}_3\text{O}_2 + \text{HO}_2 \rightarrow \text{CH}_3\text{OOH} + \text{O}_2$ $\text{CH}_3\text{OOH} + \text{OH} \rightarrow \text{CH}_2\text{O} + \text{HO}_2 + \text{OH}$	$\text{O}^{1\text{D}} + \text{N}_2 \rightarrow \text{O} + \text{N}_2$ $\text{O}^{1\text{D}} + \text{O}_3 \rightarrow 2 \text{O}_2$ $\text{O}^{1\text{D}} + \text{H}_2 \rightarrow \text{OH} + \text{H}$ $\text{O}^{1\text{D}} + \text{N}_2\text{O} \rightarrow \text{O}_2 + \text{N}_2$ $\text{ClC}_4 + \text{O}^{1\text{D}} \rightarrow 4 \text{Cl}$ $\text{CFC113} + \text{O}^{1\text{D}} \rightarrow 3 \text{Cl} + 3 \text{HF}$ $\text{HCFC22} + \text{O}^{1\text{D}} \rightarrow \text{Cl} + 2 \text{HF}$ $\text{CH}_3\text{Br} + \text{O}^{1\text{D}} \rightarrow \text{Br}$ $\text{CH}_3\text{Cl} + \text{Cl} \rightarrow 2 \text{HCl}$ $\text{CHBr}_3 + \text{OH} \rightarrow 3 \text{Br} + \text{H}_2\text{O}$ $\text{H}_2 + \text{OH} \rightarrow \text{H}_2\text{O} + \text{H}$ $\text{OH} + \text{OH} \rightarrow \text{H}_2\text{O} + \text{O}$ $\text{HO}_2 + \text{O}_3 \rightarrow \text{OH} + 2 \text{O}_2$ $\text{H} + \text{HO}_2 \rightarrow \text{H}_2 + \text{O}_2$ $\text{H}_2\text{O}_2 + \text{OH} \rightarrow \text{H}_2\text{O} + \text{HO}_2$ $\text{NO} + \text{O}_3 \rightarrow \text{NO}_2 + \text{O}_2$ $\text{NO}_2 + \text{O} \rightarrow \text{NO}_3 + \text{O}_2$ $\text{NO}_2 + \text{OH} \rightarrow \text{HNO}_3$ $\text{NO}_3 + \text{NO} \rightarrow 2 \text{NO}_2$ $\text{HNO}_3 + \text{OH} \rightarrow \text{H}_2\text{O} + \text{NO}_3$ $\text{NO}_3 + \text{OH} \rightarrow \text{NO}_2 + \text{HO}_2$ $\text{N} + \text{NO} \rightarrow \text{N}_2 + \text{O}$ $\text{Cl} + \text{O}_2 \rightarrow \text{ClOO}$ $\text{Cl} + \text{CH}_4 \rightarrow \text{HCl} + \text{CH}_3$ $\text{Cl} + \text{HO}_2 \rightarrow \text{OH} + \text{ClO}$ $\text{Cl} + \text{HOCl} \rightarrow \text{ClO} + \text{HCl}$ $\text{Cl} + \text{ClOO} \rightarrow \text{ClO} + \text{ClO}$ $\text{ClO} + \text{OH} \rightarrow \text{HCl} + \text{O}_2$ $\text{ClO} + \text{NO}_2 \rightarrow \text{ClONO}_2$ $\text{ClO} + \text{ClO} \rightarrow \text{Cl}_2 + \text{O}_2$ $\text{ClO} + \text{NO}_3 \rightarrow \text{ClOO} + \text{NO}_2$ $\text{HCl} + \text{O} \rightarrow \text{OH} + \text{Cl}$ $\text{OCIO} + \text{NO} \rightarrow \text{ClO} + \text{NO}_2$ $\text{Cl}_2 + \text{OH} \rightarrow \text{HOCl} + \text{Cl}$ $\text{ClONO}_2 + \text{Cl} \rightarrow \text{Cl}_2 + \text{NO}_3$ $\text{Cl}_2 + \text{O}^{1\text{D}} \rightarrow \text{ClO} + \text{Cl}$ $\text{Br} + \text{O}_3 \rightarrow \text{BrO} + \text{O}_2$ $\text{Br} + \text{OCIO} \rightarrow \text{BrO} + \text{ClO}$ $\text{BrO} + \text{NO} \rightarrow \text{Br} + \text{NO}_2$ $\text{BrO} + \text{ClO} \rightarrow \text{Br} + \text{ClOO}$ $\text{BrO} + \text{BrO} \rightarrow \text{Br}_2 + \text{O}_2$ $\text{HOBr} + \text{O} \rightarrow \text{BrO} + \text{OH}$ $\text{HBr} + \text{O}^{1\text{D}} \rightarrow \text{OH} + \text{Br}$ $\text{CH}_2\text{O} + \text{OH} \rightarrow \text{HCO} + \text{H}_2\text{O}$ $\text{CH}_3 + \text{O}_2 \rightarrow \text{CH}_3\text{O}_2$ $\text{CH}_3\text{O}_2 + \text{HO}_2 \rightarrow \text{CH}_3\text{OOH} + \text{O}_2$ $\text{CH}_3\text{OOH} + \text{OH} \rightarrow \text{CH}_3\text{O}_2 + \text{H}_2\text{O}$ $\text{CH}_2\text{O} + \text{NO}_3 \rightarrow \text{CO} + \text{HO}_2 + \text{HNO}_3$
---	---	--

Table A2. Heterogeneous reactions

$\text{ClONO}_2 + \text{H}_2\text{O} \rightarrow \text{HOCl} + \text{HNO}_3$	$\text{ClONO}_2 + \text{HCl}_c \rightarrow \text{Cl}_2 + \text{HNO}_3$	$\text{N}_2\text{O}_5 + \text{H}_2\text{O} \rightarrow 2\text{HNO}_3$
$\text{N}_2\text{O}_5 + \text{HCl}_c \rightarrow \text{ClONO}_2 + \text{HNO}_3$	$\text{HOCl} + \text{HCl} \rightarrow \text{Cl}_2 + \text{H}_2\text{O}$	$\text{BrONO}_2 + \text{H}_2\text{O} \rightarrow \text{HOBr} + \text{HNO}_3$
$\text{HOBr} + \text{HCl} \rightarrow \text{BrCl} + \text{H}_2\text{O}$	$\text{HOBr} + \text{HBr} \rightarrow \text{Br}_2 + \text{H}_2\text{O}$	$\text{BrONO}_2 + \text{HCl} \rightarrow \text{BrCl} + \text{HNO}_3$

Table A3. Photolysis reactions

$(*) \text{O}_2 + h\nu \rightarrow 2\text{O}$	$(*) \text{O}_3 + h\nu \rightarrow \text{O} + \text{O}_2$	$\text{O}_3 + h\nu \rightarrow \text{O}^{1\text{D}} + \text{O}_2$
$\text{HO}_2 + h\nu \rightarrow \text{OH} + \text{O}$	$\text{H}_2\text{O}_2 + h\nu \rightarrow 2\text{OH}$	$\text{NO}_2 + h\nu \rightarrow \text{NO} + \text{O}$
$\text{NO}_3 + h\nu \rightarrow \text{NO}_2 + \text{O}$	$\text{NO}_3 + h\nu \rightarrow \text{NO} + \text{O}_2$	$\text{N}_2\text{O}_5 + h\nu \rightarrow \text{NO}_2 + \text{NO}_3$
$\text{HNO}_3 + h\nu \rightarrow \text{OH} + \text{NO}_2$	$\text{HNO}_4 + h\nu \rightarrow \text{OH} + \text{NO}_3$	$\text{HNO}_4 + h\nu \rightarrow \text{HO}_2 + \text{NO}_2$
$\text{Cl}_2 + h\nu \rightarrow 2\text{Cl}$	$\text{OCIO} + h\nu \rightarrow \text{O} + \text{ClO}$	$\text{Cl}_2\text{O}_2 + h\nu \rightarrow \text{Cl} + \text{ClOO}$
$\text{HOCl} + h\nu \rightarrow \text{OH} + \text{Cl}$	$\text{ClONO}_2 + h\nu \rightarrow \text{Cl} + \text{NO}_3$	$\text{ClONO}_2 + h\nu \rightarrow \text{Cl} + \text{NO}_2 + \text{O}$
$\text{ClONO}_2 + h\nu \rightarrow \text{Cl} + \text{NO}_2$	$\text{BrCl} + h\nu \rightarrow \text{Br} + \text{Cl}$	$\text{BrO} + h\nu \rightarrow \text{Br} + \text{O}$
$\text{HOBr} + h\nu \rightarrow \text{Br} + \text{OH}$	$\text{BrONO}_2 + h\nu \rightarrow \text{Br} + \text{NO}_3$	$\text{BrONO}_2 + h\nu \rightarrow \text{BrO} + \text{NO}_2$
$\text{CH}_2\text{O} + h\nu \rightarrow \text{HCO} + \text{H}$	$\text{CH}_2\text{O} + h\nu \rightarrow \text{CO} + \text{H}_2$	$\text{CH}_3\text{OOH} + h\nu \rightarrow \text{CH}_3\text{O} + \text{OH}$
$\text{ClOO} + h\nu \rightarrow \text{O} + \text{ClO}$		

812 Appendix B. Computation of the J values

The rate of photodissociation is proportional to the in-situ amount of the species i as

$$\frac{dc_i}{dt} = J_i c_i, \tag{A1}$$

where J_i whose units are s^{-1} , is the rate of photodissociation also called the J -values or the photodissociation frequency. This rate is determined by the number of photons available at a given altitude z and wavelength λ (the solar actinic flux $F(\lambda, z, \theta)$), the ability of the species (or molecule) to absorb these photons (the absorption cross section $\sigma_i(\lambda)$) and the probability that the molecule will be photochemically destroyed following the absorption (the quantum yield $\phi_i(\lambda)$), integrated over all wavelengths

$$J_i = \int_{\lambda} \sigma_i(\lambda) \phi_i(\lambda) F(\lambda, z, \theta) d\lambda. \tag{A2}$$

The attenuation of the solar flux from the flux entering at the top of the atmosphere, $F(\lambda, \infty)$, occurs primarily from gas absorption due to O_2 and O_3 which can be computed from Beer-Lambert law

$$F(\lambda, z, \theta) = F(\lambda, \infty) \exp(-[\tau(\text{O}_2) + \tau(\text{O}_3)]), \tag{A3}$$

where τ 's are the optical depths computed as

$$\tau(\text{O}_3) = \cos^{-1} \theta \int_z^{\infty} \sigma(\text{O}_3) c_{\text{O}_3}(z') dz' \quad (\text{A4})$$

for O_3 and similarly for O_2 . The above Equations (A3,A4) assumes a plane-parallel atmosphere (valid for solar zenith angle $\theta < 75^\circ$) and that scattering is negligible.

For most constituents, photolysis occurs mainly in the near-UV spectral region, which allows a further simplification of the Equation A2. In general, this expression needs to be integrated over a sufficiently small spectral interval to capture the wavelength dependency of the absorption cross-section. But, it is possible to capture the details while reducing the computational overhead, using a *J*-table approach, where the computation is performed offline for all species in a multi-dimension parameter space. In this study, we use the look-up tables of the photodissociation rates pre-computed by the TUV photolysis calculation package [120] using a pseudo-spectral two-stream discrete ordinate method for radiative transfer [121] for five typical ozone profile. The model interpolates linearly the logarithm of the photodissociation rates in these tables as a function of geometric altitude, overhead column ozone and solar zenith angle.

Appendix C. Chemical lower boundary conditions

Table A4. Chemical lower boundary conditions

$\text{N}_2\text{O} = 322$ ppbv, $\text{CH}_4 = 1.76$ ppmv, $\text{CH}_3\text{Cl} = 544$ pptv, $\text{CH}_3\text{Br} = 10.56$ pptv
$\text{CFC-11} (\text{CFCl}_3) = 260$ pptv, $\text{CFC-12} (\text{CF}_2\text{Cl}_2) = 544$ pptv
$\text{CFC-113} = 79.333$ pptv, $\text{CFC-114} = 4.25$ pptv, $\text{CFC-115} = 4.25$ pptv
$\text{HA-1301} (\text{CBrF}_3) = 3.3$ pptv, $\text{H-1211} (\text{CBrClF}_2) = 4.62$ pptv, $\text{CCl}_4 = 100$ pptv
$\text{HCFC-22} (\text{CHClF}_2) = 170$ pptv, $\text{CH}_3\text{CCl}_3 = 45.333$ pptv, $\text{CHBr}_3 = 1.1733$ pptv
$\text{O}_3 = 20$ ppbv, $\text{O}(^1\text{D}) = 1.\text{E-}21$, $\text{O}(^3\text{P}) = 2.\text{E-}17$
$\text{H} = 2.\text{E-}22$, $\text{OH} = 1.\text{E-}15$, $\text{HO}_2 = 1$ pptv, $\text{H}_2\text{O}_2 = 2$ ppbv, $\text{H}_2 = 1.\text{E-}21$
$\text{N} = 1.\text{E-}21$, $\text{NO} = 1.\text{E-}13$, $\text{NO}_2 = 2$ pptv, $\text{NO}_3 = 3.\text{E-}14$
$\text{ClOO} = 1.\text{E-}21$, $\text{OCIO} = 4.\text{E-}15$, $\text{Cl} = 9.\text{E-}19$, $\text{ClO} = 4.\text{E-}14$
$\text{ClONO}_2 = 1.\text{E-}21$, $\text{HOCl} = 2.\text{E-}13$, $\text{Cl}_2\text{O}_2 = 6.\text{E-}21$, $\text{Cl}_2 = 1.\text{E-}21$
$\text{Br} = 3.\text{E-}18$, $\text{Br}_2 = 1.\text{E-}21$, $\text{BrO} = 7.\text{E-}16$, $\text{BrCl} = 3.\text{E-}16$, $\text{HOBr} = 3.\text{E-}15$
$\text{CH}_3 = 1.\text{E-}21$, $\text{CH}_3\text{O} = 1.\text{E-}21$, $\text{CH}_3\text{O}_2 = 1.\text{E-}21$, $\text{CH}_2\text{O} = 1.\text{E-}21$
$\text{CH}_3\text{OOH} = 0.649$ ppbv
$\text{HNO}_3 = 2$ pptv, $\text{HNO}_4 = 3.\text{E-}14$, $\text{N}_2\text{O}_5 = 2.\text{E-}14$, $\text{ClONO}_2 = 1.\text{E-}13$
$\text{BrONO}_2 = 5.\text{E-}16$
$\text{HBr} = 4.\text{E-}15$, $\text{HCl} = 1$ pptv, $\text{CO} = 15$ ppmv, $\text{HF} = 1.\text{E-}21$, $\text{HCO} = 1.\text{E-}21$
$\text{CO}_2 = 380$ ppmv

825 Appendix D. Mathematical properties of CTM and MR modes

In the MR mode, the meteorology, and in particular the wind field, is discontinuous before and after the meteorological analysis times t_A

$$\mathbf{V}(t_A^-) \neq \mathbf{V}(t_A^+). \quad (\text{A5})$$

But in off-line CTM mode, the winds are time-continuous,

$$\mathbf{V}(t_A^-) = \mathbf{V}(t_A^+). \quad (\text{A6})$$

Between analysis times, for both CTM and Meteorological Refresh modes, the evolution of the meteorology is time-continuous and the chemical tracer fields evolves as

$$\chi(t + \Delta t) = \chi(t) - \Delta t \mathbf{V}(t) \cdot \nabla \chi(t) \quad (\text{A7})$$

for each time step Δt . In the time step preceding the analysis time we have

$$\chi(t_A^-) = \chi(t_A - \Delta t) - \Delta t \mathbf{V}(t_A - \Delta t) \cdot \nabla \chi(t_A - \Delta t). \quad (\text{A8})$$

Since there is no chemical analysis increment (as we consider here that there is no chemical assimilation), the chemical concentration field is continuous at t_A , that is,

$$\chi(t_A^-) = \chi(t_A^+), \quad (\text{A9})$$

so that one time step after the analysis we have

$$\chi(t_A + \Delta t) = \chi(t_A^+) - \Delta t \mathbf{V}(t_A^+) \cdot \nabla \chi(t_A^+). \quad (\text{A10})$$

From Equation A8 we have

$$\left. \frac{d\chi}{dt} \right|_{t_A^-} = \mathbf{V}(t_A^-) \cdot \nabla \chi(t_A), \quad (\text{A11})$$

and from Equation A10 we have

$$\left. \frac{d\chi}{dt} \right|_{t_A^+} = \mathbf{V}(t_A^+) \cdot \nabla \chi(t_A), \quad (\text{A12})$$

and thus combining Equations A11, A12 we get in general

$$\left. \frac{d\chi}{dt} \right|_{t_A^+} - \left. \frac{d\chi}{dt} \right|_{t_A^-} = (\delta_A \mathbf{V}) \cdot \nabla \chi(t_A) \quad (\text{A13})$$

where $\delta_A \mathbf{V} = \mathbf{V}(t_A^+) - \mathbf{V}(t_A^-)$ which is equal to zero for a offline CTM and is equal the wind analysis increment in a coupled model run in MR mode. This result is summarized in Equation 18 in the section 5.

1. Lahoz, W. Research satellites. In *Data Assimilation: Making Sense of Observations*; Lahoz, W.; Khattatov, B.; Ménard, R., Eds.; Springer-Verlag: Berlin Heidelberg, 2010; pp. 301–321. doi:10.1007/978-3-540-74703-1_12.
2. Reber, C.A.; Trevathan, C.E.; McNeal, R.J.; Luther, M.R. The Upper Atmosphere Research Satellite (UARS) mission. *J. Geophys. Res.: Atmospheres* **1993**, *98*, 10643–10647, [https://agupubs.onlinelibrary.wiley.com/doi/pdf/10.1029/92JD02828]. doi:10.1029/92JD02828.
3. UARS Science Team; Rood, R.B.; Geller, M.A., Eds.. UARS Data and Scientific Results (Special Issue). *J. Atmos. Sci.*, **1994**, Vol. 51, 2781–3105.
4. UARS Science Team; Gille, J.C.; Massie, S.T.; Mankin, W.G., Eds.. Evaluation of the UARS Data (Special Issue). *J. Geophys. Res.: Atmospheres*, **1996**, D6, 9539–10473.
5. Louet, J. The Envisat Mission and System. http://www.esa.int/esapub/bulletin/bullet106/bul106_1.pdf, 2001.
6. Envisat Science Team. Validation Workshop Proceedings, 2002. http://http://envisat.esa.int/pub/ESA_DOC/envisat_val_1202/proceedings/.
7. MIPAS Science Team. MIPAS Geophysical Validation (Special Issue). *Atmos. Chem. Phys.*, **9**, pages = 413–442, 2002. http://envisat.esa.int/pub/ESA_DOC/envisat_val_1202/proceedings/.
8. EOS Aura (website). <http://aura.gsfc.nasa.gov/>.
9. EOS Aura Science Team. EOS Aura (Special Issue). *IEEE Transactions of Geoscience and Remote Sensing* **2006**, *44*, 1063–1379.
10. Schoeberl, M.R.; Douglass, A.R.; Joiner, J. Introduction to special section on Aura Validation. *J. Geophys. Res.: Atmospheres* **2008**, *113*, [https://agupubs.onlinelibrary.wiley.com/doi/pdf/10.1029/2007JD009602]. doi:10.1029/2007JD009602.
11. Lahoz, W.; Errera, Q. Constituent assimilation. In *Data Assimilation: Making Sense of Observations*; Lahoz, W.; Khattatov, B.; Ménard, R., Eds.; Springer-Verlag: Berlin Heidelberg, 2010; pp. 449–490. doi:10.1007/978-3-540-74703-1_18.
12. Brasseur, G.; Hauglustaine, D.; Walters, S.; Rasch, P.; Mfiller, J.; Granter, C.; Tie, X. MOZART, a global chemical transport model for ozone and related chemical tracers - 1. Model description. *J. Geophys. Res.* **1998**, *103*, 28,265–28,289.
13. Chipperfield, M.P. Multiannual simulations with a three-dimensional chemical transport model. *J. Geophys. Res.* **1999**, *104*, 1781–1805, [https://agupubs.onlinelibrary.wiley.com/doi/pdf/10.1029/98JD02597]. doi:10.1029/98JD02597.
14. Baklanov, A.; Brunner, D.; Carmichael, G.; Flemming, J.; Freitas, S.; Gauss, M.; Hov, O.; Mathur, R.; Schlunzen, K.H.; Seigneur, C.; Vogel, B. Key Issues for Seamless Integrated Chemistry–Meteorology Modeling. *Bulletin Amer. Meteorol. Soc.* **2017**, *98*, 2285–2292, [https://doi.org/10.1175/BAMS-D-15-00166.1]. doi:10.1175/BAMS-D-15-00166.1.
15. Stouffer, R.J.; Eyring, V.; Meehl, G.A.; Bony, S.; Senior, C.; Stevens, B.; Taylor, K.E. CMIP5 Scientific Gaps and Recommendations for CMIP6. *Bulletin Amer. Meteorol. Soc.* **2017**, *98*, 95–105, [https://doi.org/10.1175/BAMS-D-15-00013.1]. doi:10.1175/BAMS-D-15-00013.1.

16. Lamarque, J.F.; Emmons, L.; Hess, P.; Kinnison, D.; Tilmes, S.; Vitt, F.; Heald, C.; Holland, E.; Lauritzen, P.; Neu, J.; Orlando, J.; Rasch, P.; Tyndall, G. CAM-chem: description and evaluation of interactive atmospheric chemistry in the community earth system model. *Geosci. Model Dev.* **2012**, *5*, 369–411.
17. Marsh, D.R.; Mills, M.J.; Kinnison, D.E.; Lamarque, J.F.; Calvo, N.; Polvani, L.M. Climate Change from 1850 to 2005 Simulated in CESM1(WACCM). *J. Clim.* **2013**, *26*, 7372–7391, [<https://doi.org/10.1175/JCLI-D-12-00558.1>]. doi:10.1175/JCLI-D-12-00558.1.
18. Eyring, V.; Harris, N.; Rex, M.; Shepherd, T.; Fahey, D.; Amanatidis, G.; Austin, J.; Chipperfield, M.; Dameris, M.; Forster, P.F.; Gettelman, A.; Graf, H.; Nagashima, T.; Newman, P.; Pawson, S.; Prather, M.; Pyle, J.; Salawitch, R.; Santer, B.; Waugh, D. A Strategy for Process-Oriented Validation of Coupled Chemistry–Climate Models. *Bulletin Amer. Meteorol. Soc.* **2005**, *86*, 1117–1134, [<https://doi.org/10.1175/BAMS-86-8-1117>]. doi:10.1175/BAMS-86-8-1117.
19. SPARC CCMVal Report on the Evaluation of Chemistry–Climate Models. Technical report, SPARC, 2010.
20. Zhang, Y. Online-coupled meteorology and chemistry models: history, current status, and outlook. *Atmos. Chem. Phys.* **2008**, *8*, 2895–2932.
21. Baklanov, A.; Schlünzen, K.; Suppan, P.; Baldasano, J.; Brunner, D.; Aksoyoglu, S.; Carmichael, G.; Douros, J.; Flemming, J.; Forkel, R.; Galmarini, S.; Gauss, M.; Grell, G.; Hirtl, M.; Joffre, S.; Jorba, O.; Kaas, E.; Kaasik, M.; Kallos, G.; Kong, X.; Korsholm, U.; Kurganskiy, A.; Kushta, J.; Lohmann, U.; Mahura, A.; Manders-Groot, A.; Maurizi, A.; Moussiopoulos, N.; Rao, S.T.; Savage, N.; Seigneur, C.; Sokhi, R.S.; Solazzo, E.; Solomos, S.; Sørensen, B.; Tsegas, G.; Vignati, E.; Vogel, B.; Zhang, Y. Online coupled regional meteorology chemistry models in Europe: current status and prospects. *Atmos. Chem. Phys.* **2014**, *14*, 317–398. doi:10.5194/acp-14-317-2014.
22. Galmarini, S.; Hogrefe, C.; Brunner, D.; Baklanov, A.; Makar, P. Preface Article for the Atmospheric Environment Special Issue on AQMEII Phase 2. *Atmos. Environ.*, 115.
23. WMO CCMM. Coupled chemistry-meteorology / climate modelling (CCCM): status and relevance for numerical weather prediction, atmospheric pollution and climate research. Technical report, WMO GAW, Geneva, Switzerland.
24. von Salzen, K.; Scinocca, J.F.; McFarlane, N.A.; Li, J.; Cole, J.N.S.; Plummer, D.; Versegny, D.; Reader, M.C.; Ma, X.; Lazare, M.; Solheim, L. The Canadian Fourth Generation Atmospheric Global Climate Model (CanAM4). Part I: Representation of Physical Processes. *Atmosphere-Ocean* **2013**, *51*, 104–125. doi:10.1080/07055900.2012.755610.
25. Kunz, A.; Pan, L.; Konopka, O.; Kinnison, D.; Tilmes, S. Chemical and dynamical discontinuity at extratropical tropopause based on START08 and WACCM analyses. *J. Geophys. Res.* **2011**, *116*. doi:10.1029/2011JD016686.
26. Huijnen, V.; Flemming, J.; Chabrilat, S.; Errera, Q.; Christophe, Y.; Blechschmidt, A.M.; Richter, A.; Eskes, H. C-IFS-CB05-BASCOE: stratospheric chemistry in the Integrated Forecasting System of ECMWF. *Geosci. Model Dev.* **2016**, *9*, 3071–3091. doi:10.5194/gmd-9-3071-2016.
27. de Grandpré, J.; Ménard, R.; Rochon, Y.J.; Charette, C.; Chabrilat, S.; Robichaud, A. Radiative Impact of Ozone on Temperature Predictability in a Coupled Chemistry–Dynamics Data Assimilation System. *Mon. Wea. Rev.* **2009**, *137*, 679–692, [<https://doi.org/10.1175/2008MWR2572.1>]. doi:10.1175/2008MWR2572.1.
28. Côté, J.; S., G.; Methot, A.; Patoine, A.; M., R.; Staniforth, A. The operational CMC-MRB Global Environmental Multiscale (GEM) Model: Part I: Design considerations and formulation. *Mon. Wea. Rev.* **1998**, *126*, 1373–1395. doi:10.1175/1520-0493(1998)126<1373:TOCMGE>2.0.CO;2.
29. Errera, Q.; Fonteyn, D. Four-dimensional variational chemical assimilation of CRISTA stratospheric measurements. *J. Geophys. Res.* **2001**, *106*, 12,253–12,265.
30. Errera, Q.; Daerden, F.; Chabrilat, S.; Lambert, J.C.; Lahoz, W.A.; Viscardy, S.; Bonjean, S.; Fonteyn, D. 4D-Var Assimilation of MIPAS chemical observations: ozone and nitrogen dioxide analyses. *Atmos. Chem. Phys.* **2008**, *8*, 6169–6187.
31. Skachko, S.; Errera, Q.; Ménard, R.; Christophe, Y.; Chabrilat, S. Comparison of the ensemble Kalman filter and 4D-Var assimilation methods using a stratospheric tracer transport model. *Geosci. Model Dev.* **2014**, *7*, 1451–1465. doi:10.5194/gmd-7-1451-2014.

- 914 32. Skachko, S.; Ménard, R.; Errera, Q.; Christophe, Y.; Chabrillat, S. EnKF and 4D-Var data assimilation
915 with chemical transport model BASCOE (version 05.06). *Geosci. Model Dev.* **2016**, *9*, 2893–2908.
916 doi:doi:10.5194/gmd-9-2893-2016.
- 917 33. Chartrand, D.; de Grandpré, J.; J., M. An introduction to stratospheric chemistry: Survey
918 article. *Atmosphere-Ocean* **1999**, *37*, 309–367, [<https://doi.org/10.1080/07055900.1999.9649631>].
919 doi:10.1080/07055900.1999.9649631.
- 920 34. London, J. Radiative energy sources and sinks in the stratosphere and mesosphere. Proceedings of the
921 NATO Advanced Study Institute on Atmospheric Ozone; Aiken, A., Ed. Fed. Aviat. Admin. U.S. Dep. Trans.
922 Washington D.C., 1980, pp. 703–721.
- 923 35. Shepherd, T. The middle atmosphere. *J. Atmos. Solar-Terrestrial Phys.* **2000**, *62*, 1587–1601.
924 doi:[https://doi.org/10.1016/S1364-6826\(00\)00114-0](https://doi.org/10.1016/S1364-6826(00)00114-0).
- 925 36. Shepherd, T. Issues in Stratosphere-troposphere Coupling. *J. Meteorol. Soc. Japan. Ser. II* **2002**, *80*, 769–792.
926 doi:10.2151/jmsj.80.769.
- 927 37. Warn, T.; Warn, H. The Evolution of a Nonlinear Critical Level. *Studies in Applied Mathematics* **1978**, *59*, 37–71,
928 [<https://onlinelibrary.wiley.com/doi/pdf/10.1002/sapm197859137>]. doi:10.1002/sapm197859137.
- 929 38. McIntyre, M.; Palmer, T. Breaking planetary waves in the stratosphere. *Nature* **1983**, *305*, 593–600.
- 930 39. Waugh, D.; Plumb, R.; Atkinson, R.; Schoeberl, M.; Lait, L.; Newman, P.; Loewenstein, M.; Toohey, D.; Avallone,
931 L.; Webster, C.; May, R. Transport of material out of the stratospheric Arctic vortex by Rossby wave breaking. *J.*
932 *Geophys. Res.* **1994**, *99*, 1071–1088.
- 933 40. Homeyer, C.R.; Bowman, K.P. Rossby Wave Breaking and Transport between the Tropics and Extratropics
934 above the Subtropical Jet. *J. Atmos. Sci.* **2013**, *70*, 607–626, [<https://doi.org/10.1175/JAS-D-12-0198.1>].
935 doi:10.1175/JAS-D-12-0198.1.
- 936 41. Ménard, R.; Chang, L.P. Assimilation of Stratospheric Chemical Tracer Observations Using a Kalman
937 Filter. Part II: χ^2 -Validated Results and Analysis of Variance and Correlation Dynamics. *Mon.*
938 *Wea. Rev.* **2000**, *128*, 2672–2686, [[https://doi.org/10.1175/1520-0493\(2000\)128<2672:AOSCTO>2.0.CO;2](https://doi.org/10.1175/1520-0493(2000)128<2672:AOSCTO>2.0.CO;2)].
939 doi:10.1175/1520-0493(2000)128<2672:AOSCTO>2.0.CO;2.
- 940 42. McLandress, C.; McFarlane, N. Interactions between Orographic Gravity Wave Drag and
941 Forced Stationary Planetary Waves in the Winter Northern Hemisphere Middle Atmosphere. *J.*
942 *Atmos. Sci.* **1993**, *50*, 1966–1990, [[https://doi.org/10.1175/1520-0469\(1993\)050<1966:IBOGWD>2.0.CO;2](https://doi.org/10.1175/1520-0469(1993)050<1966:IBOGWD>2.0.CO;2)].
943 doi:10.1175/1520-0469(1993)050<1966:IBOGWD>2.0.CO;2.
- 944 43. Hines, C. Doppler-spread parameterization of gravity-wave momentum deposition in the middle
945 atmosphere. Part 1: Basic formulation. *J. Atmos. Solar-Terrestrial Phys.* **1997**, *59*, 371–386.
946 doi:[https://doi.org/10.1016/S1364-6826\(96\)00079-X](https://doi.org/10.1016/S1364-6826(96)00079-X).
- 947 44. Hines, C. Doppler-spread parameterization of gravity-wave momentum deposition in the middle atmosphere.
948 Part 2: Broad and quasi monochromatic spectra, and implementation. *J. Atmos. and Solar-Terrestrial Phys.* **1997**,
949 *59*, 387–400. doi:[https://doi.org/10.1016/S1364-6826\(96\)00080-6](https://doi.org/10.1016/S1364-6826(96)00080-6).
- 950 45. Brewer, A.W. Evidence for a world circulation provided by the measurements of helium and
951 water vapour distribution in the stratosphere. *Q. J. R. Meteorol. Soc.* **1949**, *75*, 351–363,
952 [<https://rmets.onlinelibrary.wiley.com/doi/pdf/10.1002/qj.49707532603>]. doi:10.1002/qj.49707532603.
- 953 46. Dobson, G.; Massey, H. Origin and distribution of the polyatomic molecules in the atmosphere. *Proc. R. Soc.*
954 *London. Series A* **1956**, *236*, 187–193, [<https://royalsocietypublishing.org/doi/pdf/10.1098/rspa.1956.0127>].
955 doi:10.1098/rspa.1956.0127.
- 956 47. Froidevaux, L.; Allen, M.; Berman, S.; Daughton, A. The mean ozone profile and its temperature
957 sensitivity in the upper stratosphere and lower mesosphere: An analysis of LIMS observations. *J. Geophys.*
958 *Res.* **1989**, *94*, 6389–6417, [<https://agupubs.onlinelibrary.wiley.com/doi/pdf/10.1029/JD094iD05p06389>].
959 doi:10.1029/JD094iD05p06389.
- 960 48. Ward, W.; Oberheide, J.; Reise, M.; Preusse, P.; Offerman, D. Planetary wave two signatures in CHRISTA
961 2 ozone and temperature data. In *Atmospheric Science across the Stratopause*; Siskind, D.E.; Eckermann, S.D.;

- Summers, M.E., Eds.; Geophysical Monograph Series (Book 123), AGU Press: Washington D.C., 2000; pp. 319–326.
49. Barnett, J.J.; Houghton, J.T.; Pyle, J.A. The temperature dependence of the ozone concentration near the stratopause. *Q. J. R. Meteorol. Soc.* **1975**, *101*, 245–257, [<https://rmets.onlinelibrary.wiley.com/doi/pdf/10.1002/qj.49710142808>]. doi:10.1002/qj.49710142808.
50. Haigh, J.; Pyle, J. Ozone perturbation experiments in a two-dimensional circulation model. *Q. J. R. Meteorol. Soc.* **1982**, *108*, 551–574, [<https://rmets.onlinelibrary.wiley.com/doi/pdf/10.1002/qj.49710845705>]. doi:10.1002/qj.49710845705.
51. Smith, A. Numerical simulation of global variations of temperature, ozone, and trace species in the stratosphere. *J. Geophys. Res.* **1995**, *100*, 1253–1269, [<https://agupubs.onlinelibrary.wiley.com/doi/pdf/10.1029/94JD02395>]. doi:10.1029/94JD02395.
52. Kiehl, J.; Solomon, S. On the Radiative Balance of the Stratosphere. *J. Atmos. Sci.* **1986**, *43*, 1525–1534, [[https://doi.org/10.1175/1520-0469\(1986\)043<1525:OTRBOT>2.0.CO;2](https://doi.org/10.1175/1520-0469(1986)043<1525:OTRBOT>2.0.CO;2)]. doi:10.1175/1520-0469(1986)043<1525:OTRBOT>2.0.CO;2.
53. McLinden, C.; Olsen, S.; Hannegan, B.; Wild, O.; Prather, M.; Sundet, J. Stratospheric ozone in 3-D models: A simple chemistry and the cross-tropopause flux. *J. Geophys. Res.* **2000**, *105*, 14653–14665, [<https://agupubs.onlinelibrary.wiley.com/doi/pdf/10.1029/2000JD900124>]. doi:10.1029/2000JD900124.
54. Oberheide, J.; Lehmacher, G.A.; Offermann, D.; Grossmann, K.U.; Manson, A.H.; Meek, C.E.; Schmidlin, F.J.; Singer, W.; Hoffmann, P.; Vincent, R.A. Geostrophic wind fields in the stratosphere and mesosphere from satellite data. *J. Geophys. Res.: Atmospheres* **2002**, *107*, CRI 3–1–CRI 3–18, [<https://agupubs.onlinelibrary.wiley.com/doi/pdf/10.1029/2001JD000655>]. doi:10.1029/2001JD000655.
55. De Grandpré, J.; Beagley, S.R.; Fomichev, V.I.; Griffioen, E.; McConnell, J.C.; Medvedev, A.S.; Shepherd, T.G. Ozone climatology using interactive chemistry: Results from the Canadian Middle Atmosphere Model. *J. Geophys. Res.* **2000**, *105* (D21), 26,475–26,491.
56. Morcrette, J.J. Ozone-radiation interactions in the ECMWF forecast system. Technical Report 375, European Center for Medium-Range Weather Forecasting, Reading, U.K., 2013.
57. Plumb, R.; Ko, M. Interrelationships between mixing ratios of long-lived stratospheric constituents. *J. Geophys. Res.* **1992**, *97*, 10145–10156, [<https://agupubs.onlinelibrary.wiley.com/doi/pdf/10.1029/92JD00450>]. doi:10.1029/92JD00450.
58. Holton, J. A dynamically based transport parameterization for one-dimensional photochemical models of the stratosphere. *J. Geophys. Res.* **1986**, *91*, 2681–2686, [<https://agupubs.onlinelibrary.wiley.com/doi/pdf/10.1029/JD091iD02p02681>]. doi:10.1029/JD091iD02p02681.
59. Gauthier, P.; Charette, C.; Fillion, L.; Koclas, P.; Laroche, S. Implementation of a 3D variational data assimilation system at the Canadian Meteorological Centre. Part I: The global analysis. *Atmos. Ocean* **1999**, *37*, 103–156.
60. Gauthier, P.; Tanguay, M.; Laroche, S.; Pellerin, S.; Morneau, J. Extension of the 3DVAR to 4DVAR: Implementation of 4DVAR at the Meteorological Service of Canada. *Mon. Wea. Rev.* **2007**, *135*, 2339–2354. doi:10.1175/MWR3394.1.
61. Charron, M.; Polavarapu, S.; Buehner, M.; Vaillancourt, P.A.; Charette, C.; Roch, M.; Morneau, J.; Garand, L.; Aparicio, J.; MacPherson, S.; Pellerin, S.; St-James, J.; Heilliette, S. The Stratospheric Extension of the Canadian Global Deterministic Medium-Range Weather Forecasting System and Its Impact on Tropospheric Forecasts. *Mon. Wea. Rev.* **2012**, *140*, 1924–1944, [<https://doi.org/10.1175/MWR-D-11-00097.1>]. doi:10.1175/MWR-D-11-00097.1.
62. Lin, S.J.; Rood, R. Multidimensional Flux-Form Semi-Lagrangian Transport Schemes. *Mon. Wea. Rev.* **1996**, *124*, 2046–2070, [[https://doi.org/10.1175/1520-0493\(1996\)124<2046:MFFSLT>2.0.CO;2](https://doi.org/10.1175/1520-0493(1996)124<2046:MFFSLT>2.0.CO;2)]. doi:10.1175/1520-0493(1996)124<2046:MFFSLT>2.0.CO;2.
63. Côté, J.; M., R.; Staniforth, A.; Fillion, L. A variable resolution semi-Lagrangian finite-element global model of the shallow water equations. *Mon. Wea. Rev.* **1993**, *121*, 231–243. doi:10.1175/1520-0493(1993)121<0231:AVRSLF>2.0.CO;2.

64. Girard, C.; Plante, A.; Desgagné, M.; McTaggart-Cowan, R.; Côté, J.; Charron, M.; Gravel, S.; Lee, V.; Patoine, A.; Qaddouri, A.; Roch, M.; Spacek, L.; Tanguay, M.; Vaillancourt, P.A.; Zadra, A. Staggered Vertical Discretization of the Canadian Environmental Multiscale (GEM) Model Using a Coordinate of the Log-Hydrostatic-Pressure Type. *Monthly Weather Review* **2014**, *142*, 1183–1196, [<https://doi.org/10.1175/MWR-D-13-00255.1>]. doi:10.1175/MWR-D-13-00255.1.
65. Laprise, R. The Euler Equations of Motion with Hydrostatic Pressure as an Independent Variable. *Mon. Wea. Rev.* **1992**, *120*, 197–207. doi:10.1175/1520-0493(1992)120<0197:TEEOMW>2.0.CO;2.
66. Mailhot, J.; Bélair, S.; Benoit, R.; Bilodeau, B.; Delage, Y.; Fillion, L.; Garand, L.; Girard, C.; Tremblay, A. Scientific description of the RPN physics library - Version 3.6. Technical report, Recherche en Prévision Numérique, Atmospheric Environment Service, Dorval, Québec, Canada, 1998.
67. McFarlane, N. The Effect of Orographically Excited Gravity Wave Drag on the General Circulation of the Lower Stratosphere and Troposphere. *J. Atmos. Sci.* **1987**, *44*, 1775–1800, [[https://doi.org/10.1175/1520-0469\(1987\)044<1775:TEOOEG>2.0.CO;2](https://doi.org/10.1175/1520-0469(1987)044<1775:TEOOEG>2.0.CO;2)]. doi:10.1175/1520-0469(1987)044<1775:TEOOEG>2.0.CO;2.
68. Li, J.; Barker, H. A Radiation Algorithm with Correlated- Distribution. Part I: Local Thermal Equilibrium. *J. Atmos. Sci.* **2005**, *62*, 286–309. doi:10.1175/JAS-3396.1.
69. Li, J.; Wong, J.G.D.; Dobbie, J.S.; Chýlek, P. Parameterization of the Optical Properties of Sulfate Aerosols. *J. Atmos. Sci.* **2001**, *58*, 193–209, [[https://doi.org/10.1175/1520-0469\(2001\)058<0193:POTOPO>2.0.CO;2](https://doi.org/10.1175/1520-0469(2001)058<0193:POTOPO>2.0.CO;2)]. doi:10.1175/1520-0469(2001)058<0193:POTOPO>2.0.CO;2.
70. Li, J.; Min, Q. Parameterization of the Optical Properties of Sulfate Aerosols in the Infrared. *J. Atmos. Sci.* **2002**, *59*, 3130–3140, [[https://doi.org/10.1175/1520-0469\(2002\)059<3130:POTOPO>2.0.CO;2](https://doi.org/10.1175/1520-0469(2002)059<3130:POTOPO>2.0.CO;2)]. doi:10.1175/1520-0469(2002)059<3130:POTOPO>2.0.CO;2.
71. Bäumer, D.; Lohmann, U.; Lesins, G.; Li, J.; Croft, B. Parameterizing the optical properties of carbonaceous aerosols in the Canadian Centre for Climate Modeling and Analysis Atmospheric General Circulation Model with impacts on global radiation and energy fluxes. *Journal of Geophysical Research: Atmospheres* **2007**, *112*, [<https://agupubs.onlinelibrary.wiley.com/doi/pdf/10.1029/2006JD007319>]. doi:10.1029/2006JD007319.
72. Li, J.; Ma, X.; von Salzen, K.; Dobbie, S. Parameterization of sea-salt optical properties and physics of the associated radiative forcing. *Atmos. Chem. Phys.* **2008**, *8*, 4787–4798. doi:10.5194/acp-8-4787-2008.
73. Paul, J.; Fortuin, F.; Kelder, H. An ozone climatology based on ozonesonde and satellite measurements. *J. Geophys. Res.* **1998**, *103*, 31709–31734, [<https://agupubs.onlinelibrary.wiley.com/doi/pdf/10.1029/1998JD200008>]. doi:10.1029/1998JD200008.
74. Feist, D.G.; Geer, A.J.; Müller, S.; Kämpfer, N. Middle atmosphere water vapour and dynamical features in aircraft measurements and ECMWF analyses. *Atmos. Chem. Phys.* **2007**, *7*, 5291–5307.
75. Brasseur, G.; Solomon, S. *Aeronomy of the Middle Atmosphere*; D. Reidel, 1984.
76. Sander, S.; Friedl, R.; Golden, D.; Kurylo, M.; Huie, R.; Orkin, V.; Moortgat, G.; Ravishankara, A.; Kolb, C.; Molina, M. Chemical Kinetics and Photochemical Data for Use in Atmospheric Studies. Technical Report Publication 00-3, 2003, JPL, Jet Propulsion Laboratory, Pasadena, California, 2003.
77. Lowe, D.; MacKenzie, A.R. Polar stratospheric cloud microphysics and chemistry. *J. Atmos. Solar-Terrestrial Phys.* **2008**, *70*, 13–40. doi:https://doi.org/10.1016/j.jastp.2007.09.011.
78. Errera, Q. Assimilation des observations chimiques stratosphériques CRISTA suivant la méthode variationnelle à quatre dimensions. PhD thesis, Université Libre de Bruxelles, Bruxelles, Belgique, 2002.
79. Yudin, V.; Khattatov, B. Introduction to atmospheric chemistry and constituent transport. In *Data Assimilation*; Lahoz, W.; Khattatov, B.; Ménard, R., Eds.; Springer: Berlin, Heidelberg, 2010; pp. 409–430.
80. Hairer, E.; Wanner, G. *Solving Ordinary Differential Equations II*; Springer-Verlag, 1996.
81. Press, W.H.; Teukolsky, S.A.; Vetterling, W.T.; Flannery, B.P. *Numerical Recipes in FORTRAN (2Nd Ed.): The Art of Scientific Computing*; Cambridge University Press: New York, NY, USA, 1992.
82. Sportisse, B. A review of current issues in air pollution modeling and simulation. *Comput. Geosci.* **2007**, *11*, 159–181. doi:10.1007/s10596-006-9036-4.

83. Sandu, A.; Verwer, J.; Blom, J.; Spee, E.; Carmichael, G.; Potra, F. Benchmarking stiff ode solvers for atmospheric chemistry problems, - II, Rosenbrock solvers. *Atmos. Environ.* **1997**, *31*, 3459–3472.
84. Damian, V.; Sandu, A.; Damian, M.; Potra, F.; Carmichael, G. The Kinetic PreProcessor KPP - A software environment for solving chemical kinetics. *Comput. Chem. Eng.* **2002**, *26*, 1567–1579.
85. Beljaards, A.; Bechtold, P.; Khöler, M.; Morcrette, J.J.; Tompkins, A.; Viterbo, P.; Wedi, N. Numerical schemes for parametrization. Technical report, ECMWF, Reading, U.K., 1991.
86. Beljaars, A.; Balsamo, G.; Bechtold, P.; Bozzo, A.; Forbes, R.; Hogan, R.J.; Köhler, M.; Morcrette, J.J.; Tompkins, A.M.; Viterbo, P.; Wedi, N. The Numerics of Physical Parametrization in the ECMWF Model. *Frontiers in Earth Science* **2018**, *6*, 137. doi:10.3389/feart.2018.00137.
87. Caya, A.; Laprise, R.; Zwack, P. Consequences of Using the Splitting Method for Implementing Physical Forcings in a Semi-Implicit Semi-Lagrangian Model. *Mon. Wea. Rev.* **1998**, *126*, 1707–1713, [[https://doi.org/10.1175/1520-0493\(1998\)126<1707:COUTSM>2.0.CO;2](https://doi.org/10.1175/1520-0493(1998)126<1707:COUTSM>2.0.CO;2)]. doi:10.1175/1520-0493(1998)126<1707:COUTSM>2.0.CO;2.
88. Williamson, D. Time-Split versus Process-Split Coupling of Parameterizations and Dynamical Core. *Mon. Wea. Rev.* **2002**, *130*, 2024–2041, [[https://doi.org/10.1175/1520-0493\(2002\)130<2024:TSVPSC>2.0.CO;2](https://doi.org/10.1175/1520-0493(2002)130<2024:TSVPSC>2.0.CO;2)]. doi:10.1175/1520-0493(2002)130<2024:TSVPSC>2.0.CO;2.
89. Weaver, C.; Douglass, A.; Rood, R. Thermodynamic balance of three-dimensional stratospheric winds derived from data assimilation procedure. *J. Atmos. Sci.* **1993**, *50*, 2987–2993, [[https://doi.org/10.1175/1520-0469\(1993\)050<2987:TBOTDS>2.0.CO;2](https://doi.org/10.1175/1520-0469(1993)050<2987:TBOTDS>2.0.CO;2)]. doi:10.1175/1520-0469(1993)050<2987:TBOTDS>2.0.CO;2.
90. Chipperfield, M. New version of the TOMCAT/SLIMCAT off-line chemical transport model: Intercomparison of stratospheric tracer experiments. *Q. J. R. Meteorol. Soc.* **2006**, *132*, 1179–1203. doi:10.1256/qj.05.51.
91. Gauthier, P.; Buehner, M.; Fillion, L. Background-error statistics modelling in a 3D variational data assimilation scheme: estimation and impact on the analyses. Technical report, ECMWF, reading, U.K., 1998.
92. Ridolfi, M.; Blum, U.; Carli, B.; Catoire, V.; Ceccherini, S.; Claude, H.; De Clercq, C.; Fricke, K.H.; Friedl-Vallon, F.; Iarlori, M.; Keckhut, P.; Kerridge, B.; Lambert, J.C.; Meijer, Y.J.; Mona, L.; Oelhaf, H.; Pappalardo, G.; Pirre, M.; Rizi, V.; Robert, C.; Swart, D.; von Clarmann, T.; Waterfall, A.; Wetzel, G. Geophysical validation of temperature retrieved by the ESA processor from MIPAS/ENVISAT atmospheric limb-emission measurements. *Atmos. Chem. Phys.* **2007**, *7*, 4459–4487. doi:10.5194/acp-7-4459-2007.
93. Cortesi, U.; Lambert, J.C.; De Clercq, C.; Bianchini, G.; Blumenstock, T.; Bracher, A.; Castelli, E.; Catoire, V.; Chance, K.V.; De Mazière, M.; Demoulin, P.; Godin-Beekmann, S.; Jones, N.; Jucks, K.; Keim, C.; Kerzenmacher, T.; Kuellmann, H.; Kuttippurath, J.; Iarlori, M.; Liu, G.Y.; Liu, Y.; McDermid, I.S.; Meijer, Y.J.; Mencaraglia, F.; Mikuteit, S.; Oelhaf, H.; Piccolo, C.; Pirre, M.; Raspollini, P.; Ravegnani, F.; Reburn, W.J.; Redaelli, G.; Remedios, J.J.; Sembhi, H.; Smale, D.; Steck, T.; Taddei, A.; Varotsos, C.; Vigouroux, C.; Waterfall, A.; Wetzel, G.; Wood, S. Geophysical validation of MIPAS-ENVISAT operational ozone data. *Atmos. Chem. Phys.* **2007**, *7*, 4807–4867. doi:10.5194/acp-7-4807-2007.
94. Pappalardo, G.; Colavitto, T.; Congeduti, F.; Cuomo, V.; Deuber, B.; Kämpfer, N.; Iarlori, M.; Lucia, M.; Rizi, V. Validation of MIPAS Water Vapor Products by Ground Based Measurements. *European Space Agency, (Special Publication) ESA SP* **2004**.
95. Raspollini, P.; Belotti, C.; Burgess, A.; Carli, B.; Carlotti, M.; Ceccherini, S.; Dinelli, B.M.; Dudhia, A.; Flaud, J.M.; Funke, B.; Höpfner, M.; López-Puertas, M.; Payne, V.; Piccolo, C.; Remedios, J.J.; Ridolfi, M.; Spang, R. MIPAS level 2 operational analysis. *Atmos. Chem. Phys.* **2006**, *6*, 5605–5630. doi:10.5194/acp-6-5605-2006.
96. Wang, D.Y.; Höpfner, M.; Blom, C.E.; Ward, W.E.; Fischer, H.; Blumenstock, T.; Hase, F.; Keim, C.; Liu, G.Y.; Mikuteit, S.; Oelhaf, H.; Wetzel, G.; Cortesi, U.; Mencaraglia, F.; Bianchini, G.; Redaelli, G.; Pirre, M.; Catoire, V.; Huret, N.; Vigouroux, C.; De Mazière, M.; Mahieu, E.; Demoulin, P.; Wood, S.; Smale, D.; Jones, N.; Nakajima, H.; Sugita, T.; Urban, J.; Murtagh, D.; Boone, C.D.; Bernath, P.F.; Walker, K.A.; Kuttippurath, J.; Kleinböhl, A.; Toon, G.; Piccolo, C. Validation of MIPAS HNO₃ operational data. *Atmos. Chem. Phys.* **2007**, *7*, 4905–4934. doi:10.5194/acp-7-4905-2007.

97. Wetzel, G.; Bracher, A.; Funke, B.; Goutail, F.; Hendrick, F.; Lambert, J.C.; Mikuteit, S.; Piccolo, C.; Pirre, M.; Bazureau, A.; Belotti, C.; Blumenstock, T.; De Mazière, M.; Fischer, H.; Huret, N.; Ionov, D.; López-Puertas, M.; Maucher, G.; Oelhaf, H.; Pommereau, J.P.; Ruhnke, R.; Sinnhuber, M.; Stiller, G.; Van Roozendaal, M.; Zhang, G. Validation of MIPAS-ENVISAT NO₂ operational data. *Atmos. Chem. Phys.* **2007**, *7*, 3261–3284. doi:10.5194/acp-7-3261-2007.
98. Russell III, J.M.; Gordley, L.L.; Park, J.H.; Drayson, S.R.; Hesketh, W.D.; Cicerone, R.J.; Tuck, A.F.; Frederick, J.E.; Harries, J.E.; Crutzen, P.J. The Halogen Occultation Experiment. *J. Geophys. Res.: Atmospheres* **1993**, *98*, 10777–10797, [<https://agupubs.onlinelibrary.wiley.com/doi/pdf/10.1029/93JD00799>]. doi:10.1029/93JD00799.
99. Morris, G.A.; Gleason, J.F.; Russell III, J.M.; Schoeberl, M.R.; McCormick, M.P. A comparison of HALOE V19 with SAGE II V6.00 ozone observations using trajectory mapping. *J. Geophys. Res.: Atmospheres* **2002**, *107*, ACH 10–1–ACH 10–9, [<https://agupubs.onlinelibrary.wiley.com/doi/pdf/10.1029/2001JD000847>]. doi:10.1029/2001JD000847.
100. Harries, J.E.; Russell III, J.M.; Tuck, A.F.; Gordley, L.L.; Purcell, P.; Stone, K.; Bevilacqua, R.M.; Gunson, M.; Nedoluha, G.; Traub, W.A. Validation of measurements of water vapor from the Halogen Occultation Experiment (HALOE). *J. Geophys. Res.: Atmospheres* **1996**, *101*, 10205–10216, [<https://agupubs.onlinelibrary.wiley.com/doi/pdf/10.1029/95JD02933>]. doi:10.1029/95JD02933.
101. Park, J.H.; Russell III, J.M.; Gordley, L.L.; Drayson, S.R.; Benner, D.C.; McInerney, J.M.; Gunson, M.R.; Toon, G.C.; Sen, B.; Blavier, J.F.; Webster, C.R.; Zipf, E.C.; Erdman, P.; Schmidt, U.; Schiller, C. Validation of Halogen Occultation Experiment CH₄ measurements from the UARS. *J. Geophys. Res.: Atmospheres* **1996**, *101*, 10183–10203, [<https://agupubs.onlinelibrary.wiley.com/doi/pdf/10.1029/95JD02736>]. doi:10.1029/95JD02736.
102. Lindenmaier, R.; Strong, K.; Batchelor, R.L.; Bernath, P.F.; Chabrillat, S.; Chipperfield, M.P.; Daffer, W.H.; Drummond, J.R.; Feng, W.; Jonsson, A.I.; Kolonjari, F.; Manney, G.L.; McLinden, C.; Ménard, R.; Walker, K.A. A study of the Arctic NO_y budget above Eureka, Canada. *J. Geophys. Res.: Atmospheres* **2011**, *116*, [<https://agupubs.onlinelibrary.wiley.com/doi/pdf/10.1029/2011JD016207>]. doi:10.1029/2011JD016207.
103. GEM-BACH IPY data set. <https://www.sparc-climate.org/data-centre/data-access/sparc-ipy/>. Accessed: 2014-10-20.
104. Batchelor, R.L.; Strong, K.; Lindenmaier, R.; Mittermeier, R.L.; Fast, H.; Drummond, J.R.; Fogal, P.F. A New Bruker IFS 125HR FTIR Spectrometer for the Polar Environment Atmospheric Research Laboratory at Eureka, Nunavut, Canada: Measurements and Comparison with the Existing Bomem DA8 Spectrometer. *J. Atmospheric Ocean. Technol.* **2009**, *26*, 1328–1340, [<https://doi.org/10.1175/2009JTECHA1215.1>]. doi:10.1175/2009JTECHA1215.1.
105. Batchelor, R.L.; Kolonjari, F.; Lindenmaier, R.; Mittermeier, R.L.; Daffer, W.; Fast, H.; Manney, G.; Strong, K.; Walker, K.A. Four Fourier transform spectrometers and the Arctic polar vortex: instrument intercomparison and ACE-FTS validation at Eureka during the IPY springs of 2007 and 2008. *Atmos. Meas. Tech.* **2010**, *3*, 51–66. doi:10.5194/amt-3-51-2010.
106. Rodgers, C.D.; Connor, B.J. Intercomparison of remote sounding instruments. *J. Geophys. Res.: Atmospheres* **2003**, *108*, [<https://agupubs.onlinelibrary.wiley.com/doi/pdf/10.1029/2002JD002299>]. doi:10.1029/2002JD002299.
107. Rösevall, J.D.; Murtagh, D.P.; Urban, J. Ozone depletion in the 2006/2007 Arctic winter. *Geophys. Res. Lett.* **2007**, *34*, [<https://agupubs.onlinelibrary.wiley.com/doi/pdf/10.1029/2007GL030620>]. doi:10.1029/2007GL030620.
108. Sagi, K.; Murtagh, D. A long term study of polar ozone loss derived from data assimilation of Odin/SMR observations. *Atmos. Chem. and Phys. Discuss.* **2016**, *2016*, 1–27. doi:10.5194/acp-2016-352.
109. Ostler, A.; Sussmann, R.; Patra, P.K.; Houweling, S.; De Bruine, M.; Stiller, G.P.; Haenel, F.J.; Plieninger, J.; Bousquet, P.; Yin, Y.; Saunio, M.; Walker, K.A.; Deutscher, N.M.; Griffith, D.W.T.; Blumenstock, T.; Hase, F.; Warneke, T.; Wang, Z.; Kivi, R.; Robinson, J. Evaluation of column-averaged methane in models and TCCON with a focus on the stratosphere. *Atmospheric Meas. Tech.* **2016**, *9*, 4843–4859. doi:10.5194/amt-9-4843-2016.
110. Wang, Z.; Warneke, T.; Deutscher, N.M.; Notholt, J.; Karstens, U.; Saunio, M.; Schneider, M.; Sussmann, R.; Sembhi, H.; Griffith, D.W.T.; Pollard, D.F.; Kivi, R.; Petri, C.; Velasco, V.A.; Ramonet, M.; Chen, H. Contributions

- of the troposphere and stratosphere to CH₄ model biases. *Atmos. Chem. Phys.* **2017**, *17*, 13283–13295. doi:10.5194/acp-17-13283-2017.
111. Tanguay, M.; Bartello, P.; Gauthier, P. Four-dimensional data assimilation with a wide range of scales. *Tellus* **1995**, *47A*, 974–997.
112. Laroche, S.; Gauthier, P. A validation of the incremental formulation of 4D variational data assimilation in a nonlinear barotropic flow. *Tellus* **1998**, *50A*, 557–572.
113. Koshyk, J.N.; Boville, B.A.; Hamilton, K.; Manzini, E.; Shibata, K. Kinetic energy spectrum of horizontal motions in middle-atmosphere models. *J. Geophys. Res.* **1999**, *104*, 27177–27190.
114. Batello, P. Using low-resolution winds to deduce fine structure in tracers. *Atmosphere-Ocean* **2000**, *38*, 303–320. doi:10.1080/07055900.2000.9649650.
115. Haynes, P.; Vanneste, J. Stratospheric tracer spectra. *J. Atmos. Sci.* **2004**, *61*, 161–178.
116. Bacmeister, J.; Eckermann, S.; Newman, P.; Lait, L.; Chan, K.; Loewenstein, M.; Proffitt, M.; Gary, B. Stratospheric horizontal wavenumber spectra of winds, potential temperature and tracers observed by high-altitude aircraft. *J. Geophys. Res.* **1996**, *101*, 9441–9470.
117. Gage, K.S.; Nastrom, G.D. Theoretical Interpretation of Atmospheric Wavenumber Spectra of Wind and Temperature Observed by Commercial Aircraft During GASP. *J. Atmos. Sci.* **1986**, *43*, 729–740, [https://doi.org/10.1175/1520-0469\(1986\)043<0729:TIOAWS>2.0.CO;2](https://doi.org/10.1175/1520-0469(1986)043<0729:TIOAWS>2.0.CO;2). doi:10.1175/1520-0469(1986)043<0729:TIOAWS>2.0.CO;2.
118. Waugh, D.; Plumb, R. Contour advection with surgery: A technique for investigating finescale structure in tracer transport. *J. Atmos. Sci.* **1994**, *51*, 530–540.
119. Errera, Q.; Ménard, R. Technical Note: Spectral representation of spatial correlations in variational assimilation with grid point models and application to the Belgian Assimilation System for Chemical Observations (BASCOE). *Atmos. Chem. Phys.* **2012**, *12*, 10015–10031. doi:10.5194/acp-12-10015-2012.
120. Madronich, S.; Flocke, S. The role of solar radiation in atmospheric chemistry. In *Handbook of Environmental Chemistry*; Boule, P., Ed.; Springer-Verlag: Heidelberg, Germany, 1998; pp. 1–26.
121. Toon, O.; McKay, C.; Ackerman, T.; Santhanam, K. Rapid calculation of radiative heating rates and photodissociation rates in inhomogeneous multiple scattering atmospheres. *J. Geophys. Res.* **1989**, *94*, 16287–16301.